NASA Technical Memorandum 88337

Application of a Panel Method to Wake-Vortex/Wing Interaction and Comparison with Experimental Data

Brian E. Smith and James C. Ross

(NASA-TM-88337) APPLICATION OF A PANEL METHOD TO WAKE-VORTEX/WING INTERACTION AND COMPARISON WITH EXPERIMENTAL DATA (NASA) 74 p Avail: NTIS HC A04/MF A01 CSCL 01A

N87-29461

Unclas
G3/02 0103492

September 1987

National Aeronautics and
Space Administration

NASA Technical Memorandum 88337

Application of a Panel Method to Wake-Vortex/Wing Interaction and Comparison with Experimental Data

Brian E. Smith,
James C. Ross, Ames Research Center, Moffett Field, California

September 1987

National Aeronautics and
Space Administration

Ames Research Center
Moffett Field, California 94035

CONTENTS

LIST OF TABLES

LIST OF FIGURES

SYMBOLS

A	area, m^2
AR	aspect ratio
b	span of generating wing, m
C	tunnel cross-sectional area, m^2
c	local chord, m
$\bar{c}$	average chord, m
C_L	wing lift coefficient $= \frac{L}{qS}$
C_{l_α}	lift curve slope $= \frac{dC_L}{d\alpha}$
c_l	local lift coefficient $= \frac{l}{qdA}$
C_l	rolling-moment coefficient on following wing $= \frac{M}{qSb}$
C_p	pressure coefficient $= 1 - \frac{v}{V_\infty}^2$
$C_{p_{CRIT}}$	critical pressure coefficient
dS	differential element on configuration surface
h	height of free vortex above wing, m
k	ratio of wing span to wind tunnel width
L	wing lift
l	local lift
M	rolling moment
N	number of spanwise panel columns
$\underline{n}$	unit vector normal to panel surface
P	centroid of panel on configuration surface
q	dynamic pressure, $\frac{N}{m^2}$
r	radius of vortex core, m
$\underline{r}$	length of vector from a point on a singularity sheet to the centroid of a surface panel
S	configuration surface
s	semi-span of following wing, m
v	magnitude of velocity parallel to surface panels, $\frac{m}{sec.}$
V_∞	free-stream velocity, m
V_θ	vortex tangential velocity, $\frac{m}{sec.}$
W	wake surface
x	coordinate in free-stream flow direction, m
y	coordinate perpendicular to plane-of-symmetry, m
z	coordinate perpendicular to flow direction and parallel to the $y = 0$ plane-of-symmetry, m
α	angle of attack, deg

$\Delta\alpha$	angle-of-attack correction, *deg*
δ	downwash correction factor
δ^*	boundary-layer displacement thickness
δy	width of spanwise panel column
Γ	strength of free vortex, $\frac{m^2}{sec}$
λ	ratio of major axis of wind tunnel to minor axis
Φ	total velocity potential
ϕ	perturbation velocity potential
ϕ_∞	onset flow velocity potential
ρ	air density, $\frac{kg}{m^3}$
subscripts:	
c	chord of following wing
$CORR$	corrected value
f	following wing
g	generating wing
I	interior of surface
∞	free-stream conditions
L	lower surface of panel
n	number of surface panels
P	centroid of a surface panel
U	upper surface of panel
v	vortex

Application of a Panel Method to Wake-Vortex/Wing Interaction and Comparison with Experimental Data

Brian E. Smith

and

James C. Ross

Ames Research Center

SUMMARY

The ability of the VSAERO (an acronym for Vortex Separation AERODynamics) program to calculate aerodynamic loads on wings due to interaction with free vortices was studied. The loads were calculated for various positions of a downstream following wing relative to an upstream vortex-generating wing. Calculated vortex-induced span loads, rolling-moment coefficients, and lift coefficients on the following wing were compared with experimental results of McMillan et al. and El-Ramly et al. Comparisons of calculated and experimental vortex tangential velocities were also made.

The program produced good agreement with experimental data when the following wing was located more than one following-wing chordlength from the tip vortex. The predictions deteriorated as the following wing was placed in closer proximity to the vortex. At large downstream distances from the vortex-generating wing (approximately 10 generating-wing chordlengths) the code consistently overestimated the induced rolling-moment coefficients. This was due in part to the predicted vortex tangential velocities becoming progressively larger than those measured in the experiments with increasing distance from the generating wing.

Despite strong interaction between the wake-vortex filaments and surface doublet panels, the accuracy of the calculations was in most cases independent of the panel distribution and density. Good agreement between theoretical and experimental results was obtained with a minimum of experimentation with panel arrangement.

Chapter 1

INTRODUCTION

Modifications to the existing 40- by 80-ft wind tunnel facility located at NASA Ames Research Center, when complete, will greatly enhance its aerodynamic test capability. A plan view of the new facility known as the National Full-Scale Aerodynamics Complex (NFAC) is shown in figure 1. Major changes include repowering of the drive system to increase the maximum airspeed in the 40 by 80 test section from approximately 200 to 300 knots and the addition of an 80- by 120-ft test section with an airspeed of approximately 100 knots. The conversion from the closed-circuit 40 by 80 mode to the nonreturn 80 by 120 mode is accomplished by a set of flow diversion vanes as illustrated in figure 2.

During integrated systems testing of the modified wind tunnel system, a catastrophic structural failure occurred involving the collapse of vane set 5 (fig. 2). Following this incident, a major project was undertaken to reevaluate the aerodynamic performance and structural integrity of the entire wind tunnel system. Part of this project was to obtain a reliable estimate of the aerodynamic loads on the flow-turning vanes of the wind tunnel. During operation of the 80 by 120 leg of the wind tunnel, models and full-scale aircraft in the test section generate vortex wakes which interact with these vanes to produce aerodynamic force and moment loads. Estimates of the magnitude and distribution of the forces and moments on the individual vanes due to this interaction were necessary to validate the strength of the vanes and the associated support structure.

The majority of previous theoretical and experimental work involving vortex-induced lift forces and rolling moments has been motivated by the desire to better understand and alleviate the wake-vortex hazard for aircraft. Smaller aircraft encountering the wake of heavy aircraft may experience overpowering rolling moments and/or large vertical accelerations. Many studies have been done to determine the structure and rate of decay of the wing tip vortices (refs. 1-4). Techniques for modifying the vortices so as to minimize the hazard have also been suggested (refs. 5-8). The vortex-hazard problem involves relatively large separation distances between the wake-generating aircraft and the encountering aircraft. In contrast, many vortex interaction phenomena are evident in situations where the vortex-generating surface is in close proximity to the surface affected by the vortex. Vortices shed by the fuselage of an aircraft can significantly alter the flow field around the wing and tail surfaces. Vortex wakes trailing from canard surfaces affect both the load distribution on and flow field around wings, fins, and control surfaces. Helicopter rotors also experience wake-vortex interactions. Periodic rotor blade penetration of the vortex wake shed by the preceding blade can produce significant stresses on the rotor system as well as contribute to blade-vortex interaction noise (ref. 9).

Prediction of aerodynamic loading due to an encounter with a free vortex has been attempted using several conventional steady-state flow theories. Rossow et al. (ref. 10), used strip theory and vortex-lattice theory to calculate rolling-moment coefficients on a small wing in the wake of a typical transport aircraft wing in a high-lift configuration. The calculated coefficients were compared with wind tunnel measurements. The primary assumption of strip theory is that the lift on each spanwise element is given by

$$l = C_{L_\alpha} sin\alpha \frac{1}{2} \rho {U_\infty}^2 c, \tag{1}$$

where C_{L_α} is the lift-curve slope of the wing, α is the local flow inclination caused by the presence of the free vortex, and c is the local chord of the wing. This equation was integrated across the span of the encountering wing to obtain the total rolling moment. When the lift-curve slope was assumed to be equal to 2π (the two-dimensional (2-D) value), Rossow et al. (ref. 10) predicted rolling-moment coefficients which were considerably larger than the measured values. This discrepancy occurred because the 2-D value of C_{L_α} does not account for the three-dimensional (3-D) effects caused by the finite span of the wing used in the experiment and because of the radial variation in velocity of the vortex flow field. When the 2-D value of C_{L_α} was corrected for finite aspect ratio, calculated rolling-moment coefficients were only slightly larger than the measured values.

Hancock (ref. 11) adapted lifting line theory to the problem of aerodynamic loading induced on an infinite-span wing by a free vortex. In his analysis, the wing was represented by a spanwise "bound" vortex sheet extending from $x = 0$ to $x = c$ as shown in figure 3. The wing wake was represented by a vortex sheet extending downstream from $x = c$. A streamwise vortex filament was placed at distances $\frac{h}{c} = \frac{\pi}{4}$ and $\frac{h}{c} = \frac{\pi}{2}$ above the wing. Hancock's analysis indicated that the loading on the wing has two principal components. First, the circulation about a free vortex induces an antisymmetric downwash distribution on the encountering wing; upwash on one side, and downwash on the other side. The induced asymmetric spanwise loading will tend asymptotically toward zero at large spanwise distances from the vortex. Second, the spanwise velocities induced on the upper surface of the wing by the free vortex cause a symmetric "suction" loading on the wing (fig. 4). Both types of loadings were found to be proportional to the strength of the free vortex. No solution is presented for passage of the free vortex close to the wing since velocities approach infinity near the vortex filaments.

Rossow et al. (ref. 10) used a vortex-lattice method in addition to strip theory to predict rolling-moment coefficients. Vortex-lattice theory is based on the representation of a wing by a lattice of vortex filaments which cover the area of the $z = 0$ plane representing the wing. The wake is represented by a planar extension of the chordwise vortex filaments from the region representing the wing. The approach is to solve for the vorticity distribution over the wing lattice such that the bound and trailing vortices will cancel all

free-stream velocity components normal to the surface lattice and will satisfy the Kutta condition of tangential flow at the trailing edge. Because aerodynamic surfaces are represented by a planar surface, the analysis is more accurate for thin wings having little camber than for thick wings with large camber. Nevertheless, the vortex-lattice method produced the best agreement between the theoretical and experimental results of all the analytical methods examined in reference 10.

Sophisticated analytical techniques under current development will allow more accurate computation of pressures and forces on aerodynamic surfaces due to vortex interactions. In ascending order of complexity, some of these methods include 3-D panel codes, Euler codes, and Navier-Stokes codes. Panel methods represent wing and body surfaces by an assembly of quadrilateral panels with singularities distributed over their surfaces. The details of the panel code solution methods will be presented later. Three-dimensional panel methods have an advantage over vortex lattice methods in that thickness and camber effects are included. Wakes are represented by a planar doublet sheet shed from the trailing edge of lifting surfaces in the free-stream direction. Panel methods can model some nonlinear effects such as wake roll-up and the effects of boundary-layer growth on the potential flow solutions. Viscous effects are usually ignored.

Euler codes are based on the simultaneous solution of the energy, momentum, and continuity equations governing the motion of an inviscid gas. The primary application of Euler codes is in transonic and supersonic flow analysis in which discontinuities, such as shock waves, occur in the flow field. Although more of the physics of fluid motion, i.e., compressibility are included than in linear panel methods, Euler codes require careful application of the boundary conditions at solid surfaces and at the boundaries of the computational space. The Euler equations contain no viscous terms, however, a "numerical viscosity" generally results from a discretization of the equations. The numerical viscosity and sensitivity to boundary conditions require user expertise in the application of these methods.

Navier-Stokes codes are seemingly well-suited to flow problems involving strong viscous/inviscid interactions with large regions of separated flow as the complete set of Navier-Stokes equations are solved. Because of the complexity of these equations, however, solutions are frequently impossible or at least impractical to obtain due to the large amount of computer time and memory required. For laminar flows, the equations can be simplified and solution time thereby reduced. At present, these types of calculations can be performed only on simple geometries. As computer speed and memory size increase, the range of application of the Navier-Stokes codes will broaden.

The purpose of the present investigation was to assess, by comparison with wind tunnel data, the accuracy and limitations of a panel code, VSAERO (ref. 12), when applied to wake vortex/wing interactions. VSAERO was used to model the nonlinear effects of wake vortex interaction with a following wing. The program was used to simulate experiments

of McMillan et al. (ref. 13) and El-Ramly et al. (ref. 14). The predicted values of lift and rolling moments on a wing caused by an encounter with a free vortex were compared with experimental data. The results of this study were used to validate the panel code, VSAERO, as a tool for obtaining estimates of vortex-induced aerodynamic loads on the flow turning vanes of the NFAC.

Chapter 2

DESCRIPTION OF THE VSAERO PROGRAM

VSAERO (ref. 12) is based on a surface singularity panel method using constant-strength, quadrilateral, doublet panels. The mathematical model consists of an arbitrary configuration simulated by an assembly of doublet and/or doublet and source panels surrounded by a uniform velocity of potential, ϕ_∞ (fig. 5). The sum of the onset flow potential, ϕ_∞, and the perturbation potential due to all of the panels, ϕ, gives the total velocity potential, Φ, of the external flow field. The velocity potential on the interior of the configuration is Φ_i. When Green's Theorem is applied to the regions interior and exterior to the configuration surface, and the resulting expressions are combined, we obtain an equation for the potential at a control point, P, located interior to the configuration surface a finite distance beneath the panel centroid. The equation is of the form

$$4\pi\Phi_P = \int\int_{S-P} (\Phi - \Phi_i)\underline{n} \cdot \nabla(\frac{1}{\underline{r}})dS - 2\pi(\Phi - \Phi_i)_P$$
$$+ \int\int_W (\Phi_U - \Phi_L)\underline{n} \cdot \nabla(\frac{1}{\underline{r}})dW$$
$$+ \int\int_S (\frac{1}{\underline{r}})\underline{n} \cdot (\nabla\Phi_i - \nabla\Phi)dS$$
$$+ 4\pi\phi_{\infty P}. \tag{2}$$

This equation gives the potential at P, as the sum of perturbation potentials due to a doublet distribution of strength, $(\Phi - \Phi_i)$, on the configuration surface, S, and $(\Phi_U - \Phi_L)$ on the wake surface, W, and a source distribution of strength, $\underline{n} \cdot (\nabla\Phi_i - \nabla\Phi)$, on S. The last term in the equation represents the potential for the uniform onset flow, ϕ_∞. The length of the vector from a point on the singularity sheet to P is given as $\underline{r}$.

The doublet distribution, ϕ, is obtained by imposing the internal Dirichlet boundary conditions which specify zero perturbation potential inside the configuration, i.e., $\Phi_i = \phi_\infty$. When this substitution is made, equation (2) becomes

$$0 = \int\int_{S-P} \phi\underline{n} \cdot \nabla(\frac{1}{\underline{r}})dS - 2\pi\phi_P$$
$$+ \int\int_W (\Phi_U - \Phi_L)\underline{n} \cdot \nabla(\frac{1}{\underline{r}})dW$$
$$+ \int\int_S (\frac{1}{\underline{r}})\underline{n} \cdot (\nabla\phi_\infty - \nabla\Phi)dS. \tag{3}$$

The first term in equation (3) represents the perturbation potential due to a doublet distribution of strength, ϕ, on the surface of the configuration. The second term is the contribution to outward normal velocity at point P. The third term gives the doublet distribution of strength, $\Phi_U - \Phi_L$, on the wake surface. The fourth term represents a source distribution of strength, $\underline{n} \cdot (\nabla\phi_\infty - \nabla\Phi)$, on the surface panels. Sources can be used to simulate a boundary layer by transpiration or when it is necessary to simulate an air intake or jet exhaust. One row of the matrix of influence coefficients is determined by calculating the effect at P of a unit perturbation potential placed at each of the other panel control points. Successive rows of the matrix are determined in a similar fashion for each of the other panel control points, P_n, where n is the number of surface panels. The coefficients are of the form of the integrand of the first term of equation (3). The velocity potential of the external flow field, Φ, is found by numerically solving a system of n simultaneous equations for the distribution of doublet and source values on the panel centroids.

Wakes are modeled as quadrilateral, constant-strength doublet panels. The wake surface cannot support a load; therefore, the doublet distribution on the wake surface must satisfy a zero-force condition. The doublet value of all panels in a streamwise wake column is constant and is proportional to the value of the local circulation of the surface panel column from which the wake is shed. The jump in doublet strength between adjacent columns of wake panels causes the junction to behave as a vortex filament. The wake geometry is described within the code by a set of cross-flow planes called wake-grid planes. The x-locations of these planes are specified by the user. Initially, both the surface panel doublet distribution and the final wake location are unknown. When a converged solution is obtained, the upstream edge of the wake and hence the trailing edge of the surface carries no load, and thus the trailing-edge Kutta condition will be satisfied. The program allows iterative relocation of the wake panels by aligning the streamwise edges of the wake panels with the local calculated flow direction. This wake relaxation feature is especially important in the study of the effect of lift-generated wakes on following aircraft.

The output from the code provides doublet values, nondimensional velocities and pressure coefficients at the surface panel centroids. The program computes all force and moment coefficients for both the entire configuration and specified subsections. It will calculate the paths of surface and off-body streamlines, and it will calculate the flow velocity at arbitrary or user-specified points in the flow field. Surface velocities are determined from the gradient of the doublet distribution. Pressure coefficients are referenced to a nondimensional, onset velocity arbitrarily set equal to 1 and are computed using the formula,

$$C_p = 1 - v^2. \tag{4}$$

The utility of the code is enhanced through the generation of a complete plot file of geometric and aerodynamic data.

Boundary-layer effects can be simulated using surface transpiration. A 2-D, integral boundary-layer calculation is performed along surface streamlines or on streamwise columns of panels on wing surfaces. From these calculations, the displacement thickness can be determined over the entire surface. The displacement thickness can then be simulated by surface transpiration. After the appropriate transpiration is determined for each panel, a second potential flow solution is obtained using the new boundary conditions.

Chapter 3

DESCRIPTION OF THE EXPERIMENTS OF MC MILLAN AND OF EL-RAMLY

The experiments performed by Mc Millan et al. (ref. 13) and El-Ramly et al. (ref. 14) were chosen for the present study because of their relatively simple geometries and the completeness of the data presented. The experiments provide detailed information on the aerodynamic characteristics of the wings used in the tests and on the structure and location of the tip vortices. The data also permitted a comparision with calculated results for cases involving isolated wing configurations prior to proceeding to the more difficult task of calculating vortex-induced loading on encountering wings.

The experiment by McMillan et al. (ref. 13) was performed in the 7- by 10-ft Wind Tunnel operated by the Army Air Mobility Research and Development Laboratory located at NASA Ames Research Center. The experimental arrangement used by Mc Millan is shown in figure 6. The generating wing was mounted vertically in the wind tunnel at an angle of attack of 12.6° The wing (NACA 0015, chord 18.0 in.) was of rectangular planform with an aspect ratio of 5.4. Its semi-span was 58% of the test section height. The following wing (NACA 0012, chord 3.9 in.) was mounted horizontally on the wind tunnel scale system at $\alpha = 0°$. The follower was also of rectangular planform with an aspect ratio of 8.9. It was positioned downstream of the generating-wing trailing edge, a distance of two generating-wing chordlengths. The span of the following wing was 15% of the test section width and 36% of the span of the generating wing. All data were taken at a test section velocity of 160 ft/sec.

The flow field downstream of the generating wing was measured experimentally. This was done in order to document the position and induced velocities of the tip vortex. The following wing was not present in the tunnel during these measurements and thus did not influence the vortex trajectory and strength. The mean position of the vortex was determined using a vorticity meter, a rotary device which was traversed through the test section until maximum rotational speed was detected. The vortex was assumed to be located at the point of maximum RPM. Uncertainty in the vortex position measurement was $\pm 2\%$ of the span of the following wing in the $y-$direction and $\pm 7\%$ of the chord in the $z-$direction. The tangential velocities were measured using a rapid-scanning Laser Doppler Velocimeter (LDV). When the following wing was later placed in the tunnel, its position was referenced to this unperturbed vortex position.

The following wing was oriented perpendicular to the generating wing to avoid downwash effects on the lift of the following wing. Span-loading distributions, rolling-moment coefficients, and lift coefficients induced on the following wing by the vortex wake, were measured for several distances between the wing and the location of the unperturbed vor-

tex. These distances are expressed in terms of percent of the following-wing chord, $\frac{z_v}{c_f}$. The vortex was located over the right half of the following wing. Local lift coefficients on the wing were determined by integrating pressures on the upper and lower surface of the following wing. Variation in c_l was plotted versus $\frac{2y}{b}$ for each of the wing/vortex spacings.

Two geometrically identical follower models were used in the tests. One model was used to measure lift and rolling moment through a force balance system. The uncertainties in the measurement of lift and rolling moment were $\pm 5\%$ and $\pm 3\%$, respectively. The second model was instrumented with 371 pressure taps distributed in chordwise rows on the upper and lower surfaces of the wing. Span loadings obtained from integrations of the pressure data were used to compute overall lift and rolling-moment coefficients on the model.

The experiment conducted by El-Ramly et al. (ref. 14) was performed in the 20- by 30-in., low-speed, closed-circuit wind tunnel located at Carleton University in Ottowa, Canada. The experimental arrangement is illustrated in figure 7. The semi-span vortex generating wing was mounted horizontally on the side of the test section at $\alpha = 11°$. Distributed suction was applied over the porous surface of the wall around the wing root in order to alleviate interaction with the wall boundary layer. The wing (ONERA transonic calibration model) had a quarter-chord sweep of 35°, a taper ratio of one-third, and zero twist. The semi-span of 21 in. was 70% of the test section width. The generating wing had an aspect ratio of 7.0. The following wing (NACA $64_2 - 015$, chord 1.33 in.) had a rectangular planform and an aspect ratio of 7.5. The 10 in. span was 33% of the test section width and 48% of the span of the generating wing. It was mounted horizontally at $\alpha = 0°$ on a roll balance which was in turn mounted on a horizontal and vertical traversing mechanism. Rolling-moment measurements were made at 2.5 and 5.0 generating-wing spans, b_g, downstream of the generating wing quarter-chord position. Flow-field velocity surveys were made using a nonnulling, conical, five-hole probe.

Chapter 4

RESULTS AND DISCUSSION

Comparison with Experiment Performed by McMillan et al. (ref. 13)

The procedure used in comparing the computed results with experimental data is similar for both the McMillan et al. (ref. 13) and El-Ramly et al. (ref. 14) experiments. These comparisons were done in essentially four stages. First, theory and experiment were compared for the lift characteristics of the vortex-generating wing. These comparisons are important because the span-loading distribution and the total lift on a vortex-generating wing have a large effect on the structure and strength of the wake vortex (ref. 10) which, in turn, has an effect on the interaction between the following wing and the trailing vortex. Second, the experimental and theoretical lift characteristics of the isolated following wing were compared. Both span loading and lift curve slopes were compared where possible. Third, the experimental and calculated location and tangential velocity profile of the tip vortex shed from the generating wing were compared. Finally, calculated vortex-induced span loadings, rolling-moment coefficients, and lift coefficients of the following wing were compared with the experimental results.

Vortex-Generating Wing Lift Characteristics

The aerodynamic characteristics of the generating wing used in the McMillan et al. (ref. 13) experiment were calculated using VSAERO to ensure that the calculated lift coefficient of the wing agreed with the measured lift characteristics of the wing used in the experiment. The wing was paneled with 20 spanwise panel columns and 15 chordwise panel rows. Smaller panels were used near the wing tips and near the leading edge (half-cosine spacing). Initially, a planar wake was shed from the trailing edge of the wing. Subsequent wake iterations allow the wake to roll up following streamlines in the flow field. Twenty streamwise wake panel rows were used with smaller panels placed closer to the trailing edge in a half-cosine distribution. The wake extended 2.5 spans downstream of the wing leading edge. An isometric view of the paneling scheme is shown in figure 8. The wake is shown as vortex filaments in the figure. Two complete wake-shape iterations were performed following the initial calculation which used the planar wake approximation. An isometric view of the wake after the last wake-shape cycle is shown in figure 9. Because the generating wing was mounted on the tunnel floor, an aerodynamic image system for the wing was formed by the floor surface. This image system was simulated by panelling the other half of the generating wing used in the experiment.

The generating wing was set at $\alpha = 12.6°$ during the experiment. Because the lift on the wing was not directly measured during the experiment, it was necessary to estimate the

lift coefficient of the generating wing. The procedure used in this calculation is illustrated in Appendix A. The experimental lift coefficient was estimated to be 0.888. When VSAERO was used to calculate the lift coefficient for $\alpha = 12.6°$ a value of 0.921 was obtained. By reducing the angle of attack used in the calculations by the ratio of these two lift coefficient values, the desired lift coefficient was obtained in the simulation. The revised angle-of-attack value of 12.1° was used in all subsequent calculations.

Following-Wing Lift Characteristics

Comparisons were made of experimental and calculated plots of C_L versus α for the following wing with no vortex present. For this part of the study, the following wing was paneled using 12 evenly spaced spanwise columns and 10 half-cosine spaced chordwise rows. The planar wake shed from the trailing edge was aligned with the free-stream flow. The wake extended 1.5 spans downstream of the wing leading edge. Three wake-shape iteration cycles were performed. An isometric view of the paneling scheme is shown in figure 10. The wake is shown prior to relaxation. No tunnel surfaces were simulated in this calculation because of the small size of the following wing span relative to the tunnel height. Lift coefficients were calculated with the following wing at $\alpha = 1.3, 3.2, 5.3, 7.4$, and 9.5°. The calculated values are compared with the experimental results in figure 11. The slope of the calculated lift curve is only slightly greater than the slope of the experimental lift curve. Differences between the two curves become more pronounced at higher angles of attack because viscous effects are not simulated in the analysis. Although three complete wake-shape iteration cycles were performed, the calculated lift coefficients were essentially unchanged from the first potential flow calculation to the last wake-shape cycle.

Figure 12 presents a comparison between calculated and experimental span loading curves for $\alpha = 7.4°$. Results from the the last wake-shape cycle are shown. Again little change in the span loading distribution occurred with additional iterations. Calculated local lift coefficients are in excellent agreement with the experimental results near the centerline of the wing. Only on the outer third of the wing are the calculated values significantly lower than the experimental data. The spike in the calculated c_l values near the wing tips is due to a suction peak occurring over the outermost panel column. As the flow moves from the high-pressure region on the lower surface, around the tip, and then onto the upper surface, a local area of high velocity occurs on the upper surface near the tip. Though the suction peak is not evident in the experimental span-loading curve, the phenomenon can be detected experimentally with sufficiently dense pressure taps near wing tips.

Vortex Location and Tangential Velocity Profile

To compare the computed results with the measurements of span loading, lift, and rolling moment, it was necessary to determine the location of the tip vortex from the

VSAERO calculations. This was done by including a velocity scan plane in the calculation at the downstream location of the LDV traverses. A scan plane is a user-defined grid of off-body points at which the program calculates the local velocity. In this case, the scan plane consisted of a 20 by 20 grid centered on the estimated location of the vortex. The following wing was not included in these calculations. Figure 13 is a plot of the velocity vectors in the $y-z$ plane computed at the scan plane grid points. The computed vortex location was estimated by noting the intersection of lines drawn perpendicular to the velocity vectors (i.e., the center of rotation).

The velocities obtained from the scan plane calculation allowed a comparison of the predicted and experimentally measured vortex induced velocities. Figure 14 shows this comparison. The calculated peak tangential velocities are of the same order of magnitude as the experimental values. Unevenness in the calculated curve is likely due to the influence of the discrete wake-vortex filaments. A measure of the size of a vortex is its so-called core diameter. This is defined as the distance between the velocity peaks. Outside of the core, the vortex behaves as a potential vortex with the induced velocity dropping off as $\frac{1}{r}$. Inside the core, however, viscosity plays a large role and the velocity is proportional to r. The discretization of the tip vortex in the calculation allows a very realistic velocity distribution through the rolled-up tip vortex although the predicted effective core size is somewhat larger than the measurements indicate.

Vortex-Induced Span Loading on the Following Wing

The paneling scheme and initial wake configuration used for the VSAERO simulation of the experiment are shown in figures 15, 16, and 17. The details of the paneling are described under run 1 of table 1. The following wing wake was not permitted to roll-up during the wake-shape iteration cycles. Tunnel walls were not simulated in the calculation. A typical calculation required approximately 60 sec of CPU time per wake shape iteration on the Cray X-MP computer. A typical simulation required 1230 surface panels and 880 wake panels. Figures 18, 19, and 20 show the position of the wakes after four wake-shape iteration cycles.

Figures 21 through 26 compare the experimental span loading distribution with the calculated distribution for $\frac{z_v}{c_f}$ distances ranging from 1.73 to -0.18. Calculated results are shown for wake shape iterations 1 through 4. The experimental location of the unperturbed vortex and the size of the vortex core are shown to scale in the figures. Upon examining the VSAERO results, it became clear that the section lift coefficients at some spanwise locations were incorrect. At these locations, the local pressure coefficients were either above $C_{p_{CRIT}}$ (indicative of velocities greater than sonic), all negative in sign or else substantially different between the upper and lower surfaces at the trailing edge. This last problem indicates that the Kutta condition was not accurately satisfied. The spurious pressures are most likely due to the passage of streamwise vortex filaments in the generating wing

wake close to the control points of panels on the following wing. When incorrect local c_l values were encountered, replacement values were estimated by linearly interpolating between the c_l values on either side of the incorrect values.

From figure 21 it can be seen that the span loadings calculated by VSAERO are in good agreement with the experimental results for $\frac{z_v}{c_f} = 1.73$. Calculated peak values of c_l very nearly match the experimental data. Directly beneath the vortex, the values are almost identical. The shape of the curve converged rapidly to the shape calculated at the final iteration.

Calculated and experimental span loadings for $\frac{z_v}{c_f} = 0.73$ are shown in figure 22. It can be seen that the general trend of the calculated span loads matches the experimental curve. The analysis was able to accurately predict the location of peak c_l values. The positive c_l peak was also in good agreement with the experimental values, but the peak negative value was less than that of the experiment for both the second and third iterations. From this figure it can be seen that the code required two wake-shape iteration cycles for the span-loading curve to converge to its final shape.

Span loading comparisons for $\frac{z_v}{c_f} = 0.23$ are presented in figure 23. At this position, the following wing was quite close to the vortex. Because of this, the likelihood of vortex filament/surface panel interaction increased dramatically. As a result of the analysis, the code had difficulty obtaining a reasonable span load prediction. Only at iteration 1 did the shape of the span-load curve resemble the experimental results.

The code was not able to resolve the suction peak at $\frac{y}{s} = 0.5$ which was evident in the experiment. The suction peak appears when the edge of the vortex core (where the tangential velocity is at a maximum) passes closest to the surface. The high-velocity flow causes a local low-pressure area to develop. This situation occurred experimentally at $\frac{z_v}{c_f} = 0.23$, 0.05, and -0.18.

Plots comparing calculated and experimental span loadings for $\frac{z_v}{c_f} = 0.05, -0.02$, and -0.18 are shown in figures 24 through 26. As with the previous case where the vortex core passes very close to the following wing, converged solutions were not obtained with VSAERO even after three complete wake-shape iterations.

An attempt was made to obtain satisfactory span loading curves for $\frac{z_v}{c_f} = -0.02$, a case where the wing bifurcates or splits the vortex. To decrease the likelihood of vortex filament/surface panel interaction, the spanwise panel density on the generating and following wings was reduced by a factor of two (fig. 27). Results are shown in figure 28. After one interation the results show fairly good agreement with the experimental data. The calculated curve is shifted upward by approximately 0.2. The shape of the curve calculated at iteration 2 diverged significantly from the experimental results. For $\frac{-2y}{b}$ values, the agreement is good for iteration 3. In a subsequent run, spanwise panel spacing on

the generating wing was changed from a full-cosine arrangement to even spacing (fig. 29). This change decreased the number of vortex filaments present in the rolled-up tip vortex. The follower paneling was unchanged. Results from this calculation are presented in figure 30. Reasonable agreement between theoretical and experimental results was obtained at iterations 1 and 3.

As a result of the variation in answers caused by panel scheme variation, a detailed analysis was made of the sensitivity of the code to changes in paneling representation. Seven different paneling configurations we used to compute span loadings for the case of maximum vortex/follower spacing, $\frac{z_v}{c_f} = 1.73$. Table 1 describes the details of the paneling used for each computer run. In subsequent discussions, each of these cases will be referred to as runs 1 through 7.

At $\frac{z_v}{c_f} = 1.73$, the concentration of wake vortex filaments in the tip vortex is at a large distance from the surface panels of the following wing. Thus, the only vortex filaments likely to interact with the surface panels of the following wing are those in the unrolled-up portion of the generating-wing wake.

The initial modification to the paneling scheme used in run 1 was to change the generating wing spanwise panel spacing from a full-cosine to an even distribution (fig. 31). The calculated span loadings for run 2 are shown in figure 32. Excellent agreement with experimental results was obtained over the $\frac{y}{s} < 0$ portion of the following wing span. The analysis did not produce a well-converged span-load answer over the $\frac{y}{s} > 0$ portion of the wing. Nevertheless, the span-loading trends were generally correct. In run 3, the spanwise spacing on the generating wing was changed to half-cosine with the smaller panels skewed toward the wing tip which was closest to the following wing (fig. 33). The results from the calculation using this configuration are shown in figure 34. The calculated span loadings converged to a position nearly overlaying the experimental data.

Run 4 was made with the number of chordwise rows on the following wing increased from 10 to 15 (fig. 35). The spanwise panel spacing on the generating wing was returned to the original full-cosine arrangement. As expected, little change was noted between the span loading answers obtained with this panel configuration and with that used for run 1 (fig. 36). The calculated curves closely matched the experimental results. In run 5, the chordwise panel density on both the generating and following wings was reduced from 15 to 10 rows (fig. 37). As shown in figure 38, the code was able to calculate c_l values which closely matched the experimental results over the portion of the following wing from $\frac{y}{s} = -1.0$ to $\frac{y}{s} = 0.5$. From $\frac{y}{s} = 0.5$ to $\frac{y}{s} = 1.0$ the calculated local lift coefficients were in error because of the fact that the sparse paneling cannot resolve the large gradients in spanwise loading that exist between 0.5 and 1.0.

To achieve better resolution in the span-loading curves in the spanwise region near the vortex, two runs were made in which the spanwise density of the panel columns on

the following wing was increased beneath the vortex location. The spanwise columns were divided into two regions of 12 rows each. Each region had half-cosine spacing. The first region began at the left wing tip and ended at the spanwise location of the vortex. The smaller columns were placed near the end of the region. The second region began at the vortex position and ended at the right wing tip. The smaller columns in it were placed near the beginning of the region. Fifteen chordwise rows were used. The overall effect was to create a region of high panel density beneath the location of the vortex (fig. 39). It was hoped that the high spanwise density near the vortex might resolve more detail in the steep gradient region of the experimental span loading curve beneath the vortex. The generating wing was paneled with 20 spanwise columns having full-cosine spacing and 10 chordwise rows with half-cosine spacing. In run 6, the wake panels shed from the following wing were fixed in their initial planar configuration throughout the wake-shape iteration cycles. For the first pass through the potential flow calculation, the wake from the generating wing was positioned such that the streamwise edges of the wake panels would be approximately parallel with the downwash flow direction. Both the generating and following wing wakes are planar during the first calculation step. Calculated span loadings from this first step are shown in figure 40. The shape of the curve obtained for the planar wake solution is a result of the lack of a developed vortex structure during the first calculation step. Computed span loadings from iterations 1 through 4 are also shown in the figure. The span loading results from the VSAERO calculations converged to nearly the experimental curve. Run 7 was made with the same paneling scheme as run 6. In contrast to run 6, the wake of the following wing was permitted to relax and realign itself with the local calculated flow direction. Figures 41, 42, and 43 show the position of the wakes after the final iteration. The calculated span loads from run 7 are shown in figure 44. The set of curves from this run show essentially the same characteristics as those from run 6 in which a rigid following wing wake was used. The major effect of relaxation of the following wing wake is a small downward shift of the span loading curves, especially on the right half of the wing.

Vortex-Induced Rolling Moment on the Following Wing

Utilizing the calculated c_l versus $\frac{2y}{b}$ results, total rolling-moment coefficients on the following wing were calculated. Although VSAERO calculated overall force and moment coefficients for the following wing, the calculated values were at times incorrect due to the erroneous local lift at those spanwise stations where the pressure distribution calculations were in error. As described previously, where the c_l values were in error linear interpolation was used to estimate a replacement value. Using the computed and interpolated values of c_l, the total rolling-moment coefficients, C_l, and lift coefficients, C_L, were recomputed using a programmable calculator. Appendix B presents the derivations of the equations used in these calculations.

Results from the rolling-moment calculations are compared with experiment in figures 45 and 46. Figure 45 shows the variation in rolling-moment coefficient of the following wing as a function of the distance of the wing from the location of the unperturbed vortex, $\frac{z_v}{c_f}$. It can be seen that the calculated coefficient values at $\frac{z_v}{c_f} = 1.73$ and 0.73 are in quite good agreement with the experimental data. The calculated C_l values converged at iteration 4 to a value nearly equal to the value measured with the force model in the experiment. At $\frac{z_v}{c_f} = 0.23$, only the value at the first iteration came close to the experimental value. No C_l values could be calculated for $\frac{z_v}{c_f} < 0.23$ using the paneling scheme of run 1 because of incomplete span-load curves obtained in these cases.

Figure 46 presents a comparison of measured rolling-moment coefficients with those computed from the span loading curves. The calculations were performed with the vortex located at $\frac{y_v}{c_f=1.73}$. It can be seen that though considerable variation occurred among the intermediate results, the C_l values eventually converged to answers which were quite close to the experimental values in every case except two. The different paneling schemes used in runs 1, 3, and 4 had little effect on the accuracy of the results obtained at the final iteration. When a rigid wake was used on the following wing as in run 6, the calculated C_l values were larger than when the wake was allowed to roll-up as was the case in run 7.

Vortex-Induced Lift on the Following Wing

Using corrected spanwise lift distributions, the total lift coefficient on the following wing was calculated. Comparisons between calculated and experimental C_L values for $\frac{z_v}{c_f}$ ranging from 1.73 through -0.18 are shown in figure 47. For $\frac{z_v}{c_f} = 1.73$, calculated lift coefficients converged to the value measured using the pressure model. At $\frac{z_v}{c_f} = 0.73$ all calculated C_L values were within approximately 20% of the experimental results. For $\frac{z_v}{c_f} < 0.23$, lift coefficients could not be calculated due to incomplete span loadings.

Figure 48 is a comparison of measured lift coefficients with those computed from the span loading curves from runs 1 through 7. The agreement of calculated and experimental lift coefficient values is similar to the agreement of calculated and experimental rolling-moment coefficients shown in figure 46. The results from runs 1 through 4 agree quite well with the experimental results. The recomputed lift coefficients from runs 6 and 7 show a trend opposite to that of the rolling-moment coefficients from the same runs. In run 6, where the follower wake was held rigid, the lift coefficients were generally lower than those in run 7, in which the wake panels were allowed to roll-up.

Comparison with Experiment Performed by El-Ramly et al. (ref. 14)

The experiment of El-Ramly et al. (ref. 14) was performed in the 20 by 30 in. wind tunnel located at Carleton University in Canada. In the experiment, the ratio of the vortex-

generating wing area to the wind tunnel cross-sectional area was approximately three times greater than the same ratio for the experiment performed by McMillan et al. (ref. 13). Because of this, an analysis was made of the angle-of-attack corrections required caused by wind tunnel wall effects for the geometry of each experiment. The procedure used is described in Appendix C. It was determined that the generating wing/tunnel geometry of the experiment performed by El-Ramly et al. (ref. 14) requires an angle-of-attack correction per unit lift coefficient of $1.35°/C_L$. This value is almost two and one-half times the $0.58°/C_L$ correction necessary for the McMillan experiment (ref. 13). Because of this, tunnel walls were included in the VSAERO simulation of the experiment performed by El-Ramly et al. (ref. 14).

The VSAERO code permits the analysis of potential flow in ducts. The mass flow through a duct is controlled by specifying the normal velocities on the panels terminating the duct. The tunnel used in the experiment was paneled as a long duct terminated by a grid of panels with a prescribed normal velocity. The duct is shown in figure 49. The specified normal velocity on the panel grid at the near end of the duct controls the mass flow through the duct. Only three sides of the duct were paneled. The $y = 0$ reflection plane was used to simulate the fourth side of the tunnel.

In VSAERO, flow is prevented from occurring inside the surface of a configuration. Because of this, the duct (whose interior surface is in reality an exterior surface relative to the flow) was surrounded by an outer body of surface panels as shown in figure 50. The inner duct and outer body were joined at an acute angle at the front to prevent flow distortion in the forward portion of the duct because of stagnation occurring on the outer body. The outer body was placed at least one panel diameter away from the inner duct to avoid significant interaction between the inner and outer body panels (figs. 51 and 52).

Vortex-Generating Wing Span Loading

The nondimensionalized experimental span loading of the generating wing at $\alpha = 6.25°$ was compared with the results of a VSAERO calculation at the same angle of attack as shown in figure 53. Ten spanwise panel columns were used in a half-cosine arrangement with the smaller panels near the tip. Fifteen chordwise rows were used also in a half-cosine spacing with the smaller panels near the leading edge. Twenty streamwise wake panel rows were used. The wake extended 11 chords downstream of the root quarter-chord point. Figure 54 shows the initial wing/wake geometry. No attempts were made to optimize the paneling schemes used in the simulations of the El-Ramly et al. (ref. 14) experiment. The span-loading calculations were done both with and without the wing enclosed by the simulated wind tunnel. As shown in figure 53, the calculated loadings are approximately 10% lower than the experimental values near the root of the wing. Near the tip, the calculated loadings are slightly higher than the measured values. This discrepancy could be due to the use of excessive distributed suction on the tunnel side

wall during the experiment or may result from the boundary-layer-induced spanwise flow in the experiment which VSAERO does not simulate. When tunnel walls were included, the outboard portion of the wing became more highly loaded than when the span loads were calculated with the wing alone. The total lift coefficients were also calculated for cases with and without the simulation of tunnel walls. These values are compared with the experimentally determined lift coefficient in the figure. As expected, the code predicts a larger total lift coefficient when tunnel walls are simulated.

Generating- and Following-Wing Lift Characteristics

A comparison of the theoretical and experimental lift curves for the generating is shown in figure 55. The experimental lift coefficients of the generating wing were calculated by El-Ramly et al. (ref. 14) from an integration of pressures measured on the upper and lower surfaces of the wing. The theoretical lift curve for the generating wing was obtained using simulated wind tunnel walls. The slope of the experimental lift curve of the generating wing decreases above approximately $\alpha = 6°$ due to the onset of flow separation.

Figure 56 presents a comparison of the theoretical and experimental lift curves for the following wing. The lift of the following wing was measured experimentally using a three-component, external balance. Because the following wing area was small in relation to the area of the tunnel cross-section, tunnel walls were not included in the calculation of the lift curve of the wing. The following wing was paneled using 15 spanwise panel columns spaced evenly across the span. Ten chordwise panel rows were used in a half-cosine arrangement with the smaller panels near the leading edge. For the following wing, the slope determined from the experiment begins to decrease above approximately $\alpha = 7°$. The theoretical lift curves of both the generating and following wings are steeper than the experimental curves. It is clear from the figures that the code consistently overestimates the lift coefficient for a given angle of attack.

Vortex Tangential Velocity Profile

El-Ramly et al. (ref. 14) measured the total pressure and the mean velocity magnitude and direction were measured in the flow behind the vortex-generating wing using a conical, five-hole probe. These measurements were used to generate contours of equal total pressure loss and to measure the trailing vortex tangential velocities. The theoretical velocity distributions at the location of the experimental measurements were determined by use of a velocity scan plane as described previously. Figure 57 is a vector plot of the velocity vectors computed in a plane perpendicular to the flow at 2.5 generating-wing spans, b_g, downstream of the root quarter-chord point. The location of the vortex core was estimated from an examination of the y and z-components of velocity along each horizontal line. the vertical location of line 13 (counting from the top). At $x = 2.5b_g$, the vertical location of the

vortex was estimated to be at $\frac{z_v}{c_f} = -1.4$. Figure 58 is a vector plot of the velocities along line 13. Because some of the velocity vectors outboard of the immediate core area were not perpendicular to the scan line, it was concluded that the calculated vortex shape was not axisymmetric. To determine the true tangential velocities of the vortex, the resultants of the y and the z-components of velocity were computed along the scan line.

Figure 59 presents a comparison of the calculated vortex tangential velocities at $x = 2.5b_g$ with those measured during the experiment. The calculated velocities in the region from $\frac{r}{b_g} = 0.2$ to $\frac{r}{b_g} = 0.15$ were approximately 30% higher than the measured velocities. In this region, the downwash velocities were asymptotic to the value of the downwash velocity of the generating wing. The calculated velocity peak to the right of center was somewhat greater than the experimental value. The calculated peak to the left of center was smaller than the experimentally measured peak by approximately the same amount. From $\frac{r}{b_g} = -0.02$ to $\frac{r}{b_g} = -0.15$, the calculated velocities were as much as 50% higher than the experimental results. As expected, in this region the velocities were asymptotic to zero. When the vortex core size is defined to be the distance between the velocity peaks on either side of the vortex center, it can be seen from the figure that the size of the core based on VSAERO results is on the order of twice the experimental size.

Figure 60 is a vector plot of the vortex velocities at the $x = 5.0b_g$ downstream station. The location and dimensions of the scan plane used in this calculation were the same as in the calculation done at $x = 2.5b_g$. The vortex was estimated to be near line 18, at $\frac{z_v}{c_f} = -2.0$. Figure 61 presents a comparison of the calculated versus experimental tangential velocities at the downstream station, $x = 5.0b_g$. At this location, both the calculated and experimental velocity peaks were lower than at $x = 2.5b_g$. Outside of the core area, the calculated velocities were much higher than the velocities at $x = 2.5b_g$. The code overestimated the size of the core by a factor of two.

Rolling-Moment Variation with Follower Position

The rolling moment induced on the following wing by the trailing vortex was measured by El-Ramly et al. (ref. 14) at two downstream stations, $x = 2.5b_g$ and $x = 5.0b_g$. The angles of attack of the generating wing were $\alpha = 5°$ and $\alpha = 11°$ which resulted in C_L's on the wing of 0.36 and 0.74, respectively. To evaluate the code in the most linear portion of the experimental lift curve, the VSAERO simulations of the experiment were done with the generating wing set at an angle of attack which produced a calculated C_L equal to 0.359. The generating-wing wake was allowed to roll-up in the calculation while the wake shed from the following wing was held rigid during the wake-shape iteration procedure. Two wake-shape iterations were performed for each angle of attack.

In the experiment, the vertical position of the following wing was referenced to the vertical centerline of the test section. Since no data was available describing the trailing

vortex position, it was not possible to precisely duplicate the experimental spacing between the vortex and the following wing as was the case in the simulations of the experiment of reference 13. Comparison of the VSAERO calculations with the results of the El-Ramly et al. (ref. 14) experiment is a test of the capability of the code to accurately determine the shape and path of the rolled-up wake as well as to properly predict the vortex-induced loads.

In the experiment of reference 7, vertical traverses of the instrumented following wing were made at each of the two downstream stations. The traverses were made at successive lateral positions across the test section. Induced rolling moments on the follower were measured continuously during the traverses. Because of the large amount of computer time which would have been required to obtain answers at all of the traverse positions, calculations were made only at the lateral traverse position at which the maximum rolling moment was measured. The horizontal position of these traverses was 4.64 in. outboard of the test section centerline. Rolling-moment coefficients were calculated at -4, -2, 0, 2, and 4 in. above the tunnel centerline along the experimental traverse line.

Figure 62 presents a comparison between the calculated and experimental rolling-moment coefficients at the $x = 2.5b_g$ station as a function of the vertical position of the following wing. The maximum rolling moments occur at the vertical location of the shed vortex. It is apparent from the figure that the calculated location of the vortex is substantially lower than that implied by the experimental data. This may be due to inaccurate simualtion of wind tunnel wall effects in the simulation. Since the code over-estimated the tangential vortex velocities, the peak calculated rolling-moment coefficients are about 25% larger than the measured values. The overall shapes of the calculated and experimental curves are quite similar. Figure 63 shows a comparison of the calculated versus experimental C_l values at the downstream station, $x = 5.0b_g$. At this station, the calculated trailing vortex was located at $\frac{z_v}{c_f} \approx -2.0$. From the figure it can be seen that the code was able to more closely match the experimental results for $\frac{z_v}{c_f} < 0$. As at $x = 2.5b_g$, the program overestimated both the peak rolling moment and the location of the vortex path.

Chapter 5

CONCLUSIONS

The accuracy of predicted vortex-induced loads on wings by the panel code, VSAERO, was found to be dependent on the distance between the following wing and the generating wing and on the distance between the following wing and the vortex. The code produced better agreement with experimental data when the wing was farther than one following-wing chordlength from the vortex than when the wing was close to or intersected the trailing vortex. When the position of the following wing was referenced to the known location of the vortex, good agreement was observed between theoretical and experimental span loads, rolling-moment coefficients, and lift coefficients of the following wing. When the following wing was at a large distance downstream from the generating wing (8.75 and 17.5 generating-wing chordlengths), the code consistently overestimated the induced rolling-moment coefficients. For these cases, the predicted vortex tangential velocities became progressively larger than the experimental values with increasing distance from the generating wing. Inaccurate calculation of the vortex tangential velocities and of the vortex path caused the theoretical rolling-moment coefficients to be in error. When the presence of wind tunnel walls was included in the simulation, the code consistently underestimated the lift on wings and overestimated the deflection of the tip vortex caused by downwash effects. The addition of the wind tunnel walls to the simulation did not improve agreement between theory and experiment.

The accuracy of the calculations was in most cases independent of the surface panel distribution and density. Where good agreement between theoretical and experimental loads was obtained, a minimum of experimentation with panel arrangement was required. Best results were achieved with low wake-column density in the unrolled-up portion of the vortex wake which cut through the surface panels of the following wing.

Future modifications of VSAERO that would make it more useful for wake-vortex research should include a study of the effects of changes in the wake-grid plane distribution on the calculated pressure distributions on wings in vortex wakes. Comparisons between theory and experiments would be enhanced by more accurate modeling of lifting surfaces and vortex wake paths in internal flows.

APPENDIX A

Estimation of Generating Wing C_L

The lift coefficient of the vortex-generating wing used by McMillan et al. (ref. 13) was estimated by use of the formula,

$$C_L = C_{L_\alpha}\alpha, \tag{5}$$

where C_L is the lift coefficient of the wing, C_{L_α} is the lift-curve slope, and α is the angle of attack of the airfoil expressed in radians.

Jones and Cohen (ref. 15) developed a formula for determining the lift-curve slope value for finite aspect ratio wings. This formula is given by

$$C_{L_\alpha} = \frac{2\pi}{1 + \frac{3}{AR}}, \tag{6}$$

where AR is the aspect ratio of the wing.

The aspect ratio of the vortex-generating wing used in the experiment was 5.39. Substituting into equation (6),

$$C_{L_\alpha} = \frac{2\pi}{1 + \frac{3}{5.39}},$$

we obtain

$$C_{L_\alpha} = 4.036/radian.$$

The angle of attack used in the experiment was 12.6°. When this value is converted to radians and substituted into equation (5),

$$C_L = 4.036/rad(12.6deg)(\frac{\pi}{180}rad/deg),$$

we obtain

$$C_L = 0.888.$$

The value of the lift coefficient of the generating wing was then calculated using VSAERO. The calculated value of C_L was found to be 0.921 at $\alpha = 12.6°$. When the angle of attack used in the VSAERO calculations was reduced by a ratio of α_{exp} to α_{VSAERO},

$$\alpha_{corr} = \frac{0.888}{0.921}(12.6°),$$

the corrected angle of attack became

$$\alpha_{corr} = 12.143^{\circ}.$$

To verify this correction, the lift coefficient was recalculated with VSAERO using α_{corr}. The C_L value obtained in this calculation was 0.872. This value matched the estimated experimental C_L well enough that additional refinements to the calculation were considered unnecessary. The corrected angle of attack was used in all subsequent VSAERO simulations of the experiment performed by McMillan et al. (ref. 13).

APPENDIX B

Derivation of C_l and C_L Equations

The rolling-moment coefficient on a wing is given by

$$C_l = \frac{M}{qSb}, \tag{7}$$

where C_l is the rolling-moment coefficient, M is the applied moment, q is the dynamic pressure, S is the wing area, and b is the wing span.

Substituting $\int lydy$ for M, we obtain

$$C_l = \frac{\int lydy}{qSb}, \tag{8}$$

where l is the local lift on the wing, and y is the moment arm of this lift measured from mid-span.

For a constant-chord wing $\int lydy$ may be approximated by

$$\sum_{i=1}^{N} c_{l_i} c\delta y_i y_i,$$

where N is the number of spanwise panel columns on the wing, c_{l_i} is the local lift coefficient, $c\delta y_i$ is the local area of the spanwise column, and y_i is the moment arm of this section measured from the mid-span position. Substituting into equation (8) we obtain:

$$C_l = \frac{\sum_{i=1}^{N} c_{l_i} c\delta y_i y_i}{Sb}. \tag{9}$$

Substituting $S = c2(\frac{b}{2})$ and $b = 2(\frac{b}{2})$ and nondimensionalizing δy_i and y_i by $\frac{b}{2}$ we obtain

$$C_l = \frac{\sum_{i=1}^{N} c_{l_i} \delta y_i y_i}{b^2}, \tag{10}$$

where δy_i is defined as the difference between y_i and y_{i+1}. The total rolling-moment coefficients we recalculated for each complete spanloading curve using this formula on a programmable calculator.

For the lift coefficient of a constant-chord wing, it can be shown that

$$C_L s = \sum_{i=1}^{N} C_{L_i} c \delta y_i. \tag{11}$$

Solving for C_L and simplifying, we obtain

$$C_L = \frac{\sum_{i=1}^{N} C_{L_i} \delta y_i}{b}. \tag{12}$$

The same panel column data used to compute the rolling-moment coefficients was stored in memory and used to compute the total lift coefficients.

APPENDIX C

Wind-Tunnel Wall Correction

The relative magnitudes of the downwash correction factors for the four wings used in the experiments were estimated using the method outlined in chapter 6 of Pope's, Wind Tunnel Testing (ref. 18). From equation 6:14 on page 225 we have

$$\Delta\alpha = \delta\frac{S}{C}C_L \quad radians, \tag{13}$$

where δ is determined from figure 6:23 on page 237, S is the wing area, and C is the tunnel cross-sectional area.

For the McMillan et al. (ref. 13) vortex-generating wing, with

$$\lambda = \frac{major\ axis\ of\ jet}{minor\ axis\ of\ jet}, \tag{14}$$

$$\lambda = 0.7$$

and,

$$k = \frac{span}{jet\ width}, \tag{15}$$

$$k = 0.58,$$

we enter figure 6:23 to obtain

$$\delta \approx 0.117.$$

Substituting into the equation for $\Delta\alpha$ and converting to degrees, we obtain per unit lift coefficient for the McMillan generator:

$$\Delta\alpha = 0.58 \quad deg/C_L$$

When this procedure was performed on each of the other wings used in the experiments, the results were:

McMillan et al. (ref. 13) follower, $\Delta\alpha = 0.095$ *deg*
El-Ramly et al. (ref. 14) generator, $\Delta\alpha = 1.35$ *deg*
El-Ramly et al. (ref. 14) follower, $\Delta\alpha = 0.17$ *degw*

For the purpose of calculating the aerodynamic characteristics of the wings, only the correction factor calculated for the El-Ramly et al. (ref. 14) generator was large enough to require the simulation of wind tunnel walls.

REFERENCES

1. Rossow, V. J.: On the Inviscid Rolled-Up Structure of Lift-Generated Vortices. J. Aircraft, vol.10, no. 11, Nov. 1973, pp. 647-650.

2. Chigier, N. A.; and Corsiglia, V. R.: Tip Vortices-Velocity Distributions. NASA TMX 62087, 1971.

3. Corsiglia, V. R.; Schwind, R. G.; and Chigier, N. A.: Rapid Scanning, Three-Dimensional Hot-Wire Anemometer Surveys of Wing Tip Vortices. J. Aircraft, vol. 10, no. 12, Dec. 1973, pp. 752-757.

4. Chigier, N. A.: Experimental Studies of Turbulent Aircraft Wake. Israel J. Technology, vol. 11, no. 6, 1973, pp. 367-372.

5. Corsiglia, V. R.; Rossow, V. J.; and Ciffone, D. L.: Experimental Study of the Effect of Span Loading on Aircraft Wakes. J. Aircraft, vol. 13, no. 12, Dec. 1976, pp. 968-973.

6. Rossow, V. J.: Experimental Investigation of Wing Fin Configurations for Alleviation of Vortex Wakes of Aircraft. NASA TM 78520, 1978.

7. Iversen, J.; and Moghadam, M.: Experimental Investigation of Vortices Shed by Various Wing Fin Configurations. Final Report, Langley Research Center Grant no. NSG 1582, Jan. 1981.

8. Corsiglia, V. R.; Jacobsen, R. A.; and Chigier, N. A.: An Experimental Investigation of Trailing Vortices Behind a Wing with a Vortex Dissipator. Aircraft Wake Turbulence and Its Detection, Plenum Press, New York, 1971, pp. 229-242.

9. Ham, N. D.: Some Conclusions from an Investigation of Blade-Vortex Interactions. J. AHS, vol. 20, no. 4, Oct. 1975, pp. 26-31.

10. Rossow, V. J.; Corsiglia, V. R.; Schwind, R. G.; Frick, J. K. D.; and Lemmer, O. J.: Velocity and Rolling-Moment Measurements in the Wake of a Swept-Wing Model in the 40-by 80-Foot Wind Tunnel. NASA TMX 62414, Apr. 1975.

11. Hancock, G. J.: Aerodynamic Loading Induced on a Two- Dimensional Wing by a Free Vortex in Incompressible Flow. Aeronaut. J. Royal Aeronaut. Society, vol. 75, June 1971, pp. 413-416.

12. Maskew, B.: Program VSAERO, A Computer Program for Calculating the Non-Linear Characteristics of Arbitrary Configurations. NASA CR 166476, 1972.

13. McMillan, O. J.; Schwind, R. G.; Nielsen, J. N.; and Dillenius, M. F. E.: Rolling Moments in a Trailing Vortex Flow Field. NASA CR 151961, 1977.

14. El-Ramly, Z.; Rainbird, W. J.; and Earl, D. G.: Wind Tunnel Measurements of Rolling Moment in a Swept Wing Wake. J. Aircraft, vol. 13, no. 12, Dec. 1976, pp. 962-967.

15. Jones, R. T.; and Cohen, D.: Aerodynamics of Wings at High Speeds. High Speed Aerodynamics and Jet Propulsion, vol. 7, Princeton University Press, Princeton, New Jersey, 1957, p. 95.

16. Patel, M. H.; and Hancock, G. J.: Some Experimental Results of the Effect of a Streamwise Vortex on a Two-Dimensional Wing. Aeronaut. J. Royal Aeronaut. Society, vol. 78, Apr. 1974, pp. 151-155.

17. El-Ramly, Z.; and Rainbird, W. J.: Flow Survey of the Vortex Wake behind Wings. J. Aircraft, vol. 14, no. 11, Nov. 1977, pp. 1102-1108.

18. Pope, A.: Wind Tunnel Testing. John Wiley and Sons, New York, 1947, pp. 225-237.

19. Rossow, V. J.: Survey of Computational Methods for Lift- Generated Wakes. NASA SP 347, 1975, pp. 897-913.

TABLE 1. PANELING SCHEMES USED ON THE GENERATING AND FOLLOWING WINGS

RUN NUMBER	VORTEX-GENERATING WING				FOLLOWING WING			
	SPANWISE COLUMNS	SPACING	CHORDWISE ROWS	WAKE SPECIFICATION	SPANWISE COLUMNS	SPACING	CHORDWISE ROWS	WAKE SPECIFICATION
1	20	FULL-COSINE	15	FLEXIBLE	24	EVEN	10	RIGID
2	20	EVEN	15	FLEXIBLE	24	EVEN	10	RIGID
3	20	HALF-COSINE	15	FLEXIBLE	24	EVEN	10	RIGID
4	20	FULL-COSINE	15	FLEXIBLE	24	EVEN	15	RIGID
5	20	FULL-COSINE	10	FLEXIBLE	24	EVEN	10	RIGID
6	20	FULL-COSINE	10	FLEXIBLE	12 12	HALF-COSINE	15	RIGID
7	20	FULL-COSINE	10	FLEXIBLE	12 12	HALF-COSINE	15	FLEXIBLE

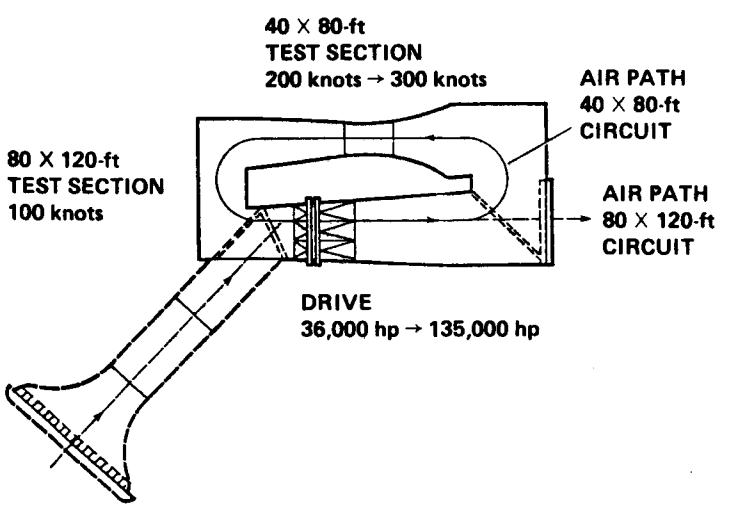

Figure 1.– Plan View of the NFAC.

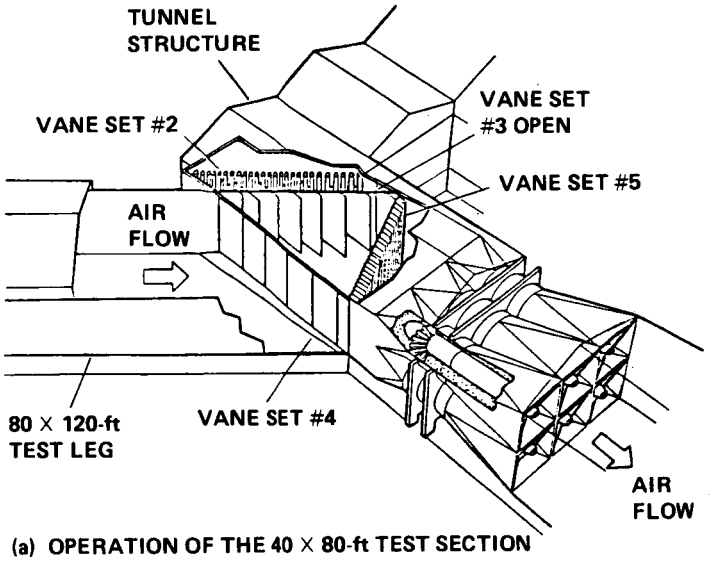

(a) OPERATION OF THE 40 X 80-ft TEST SECTION

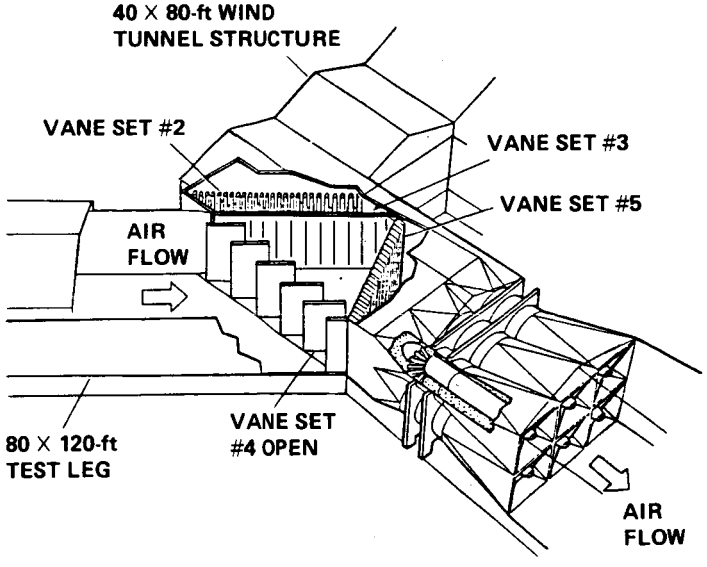

(b) OPERATION OF THE 80 X 120-ft TEST SECTION

Figure 2.– Flow Diversion Vanes of the NFAC.

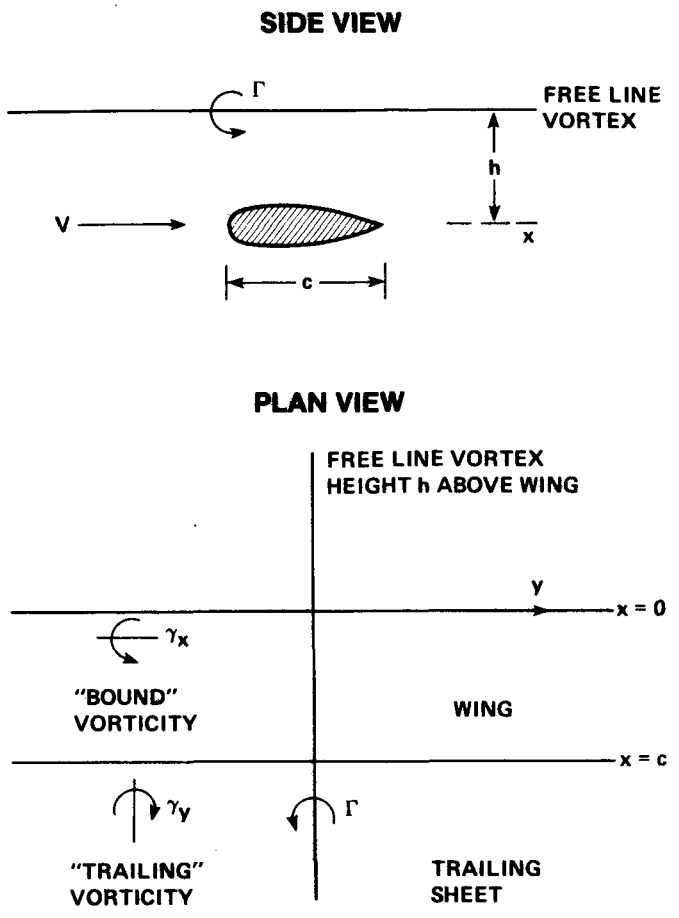

Figure 3.– Flow-Field Model used by Hancock.

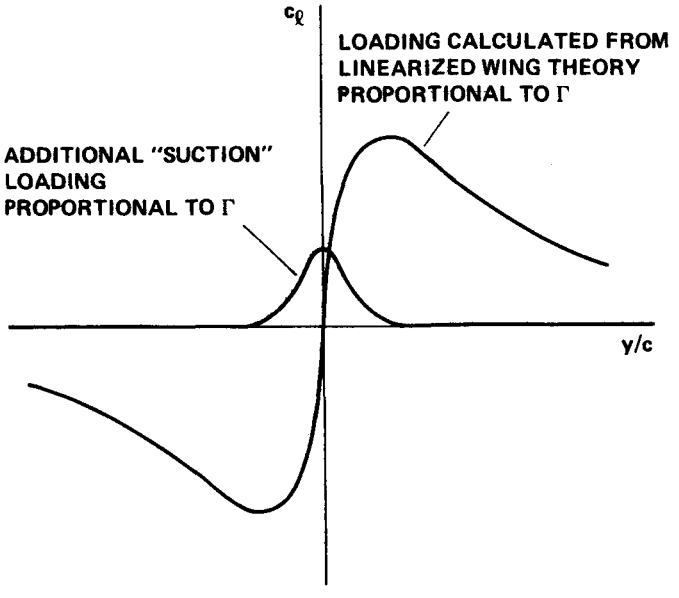

Figure 4.– Spanwise-Load Distribution Characteristics.

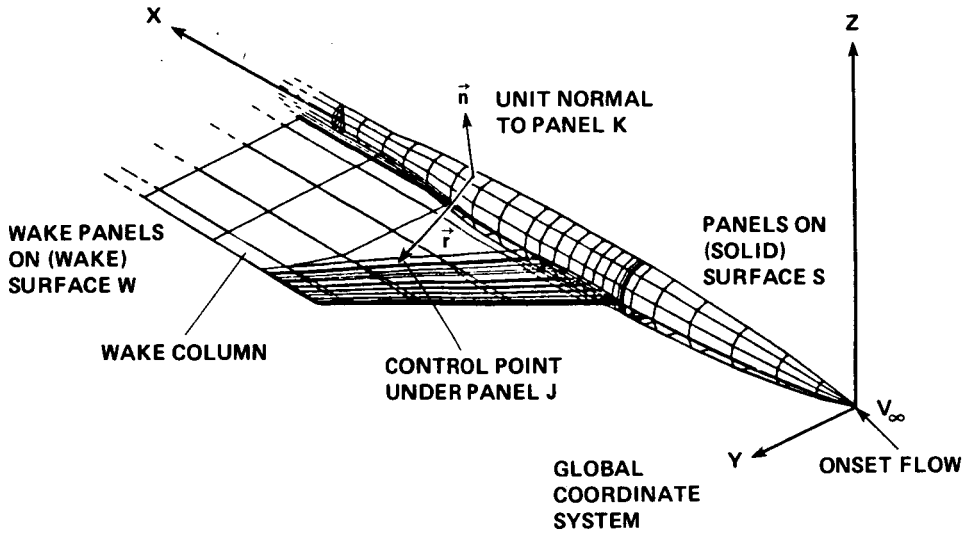

Figure 5.– Example of a Paneled Configuration.

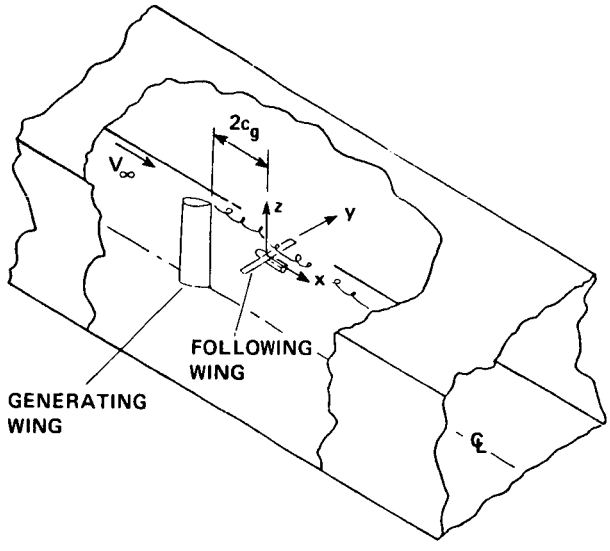

Figure 6.– Experimental Arrangement used by McMillan et al. (ref. 13).

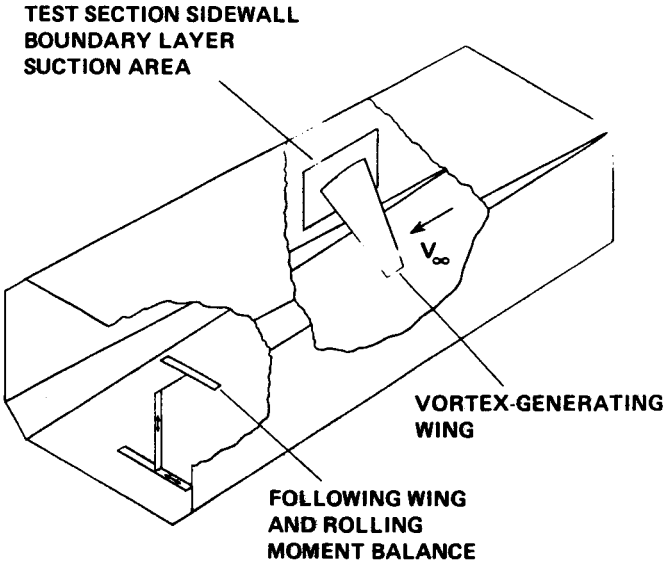

Figure 7.- Experimental Arrangement used by El-Ramly et al. (ref. 14).

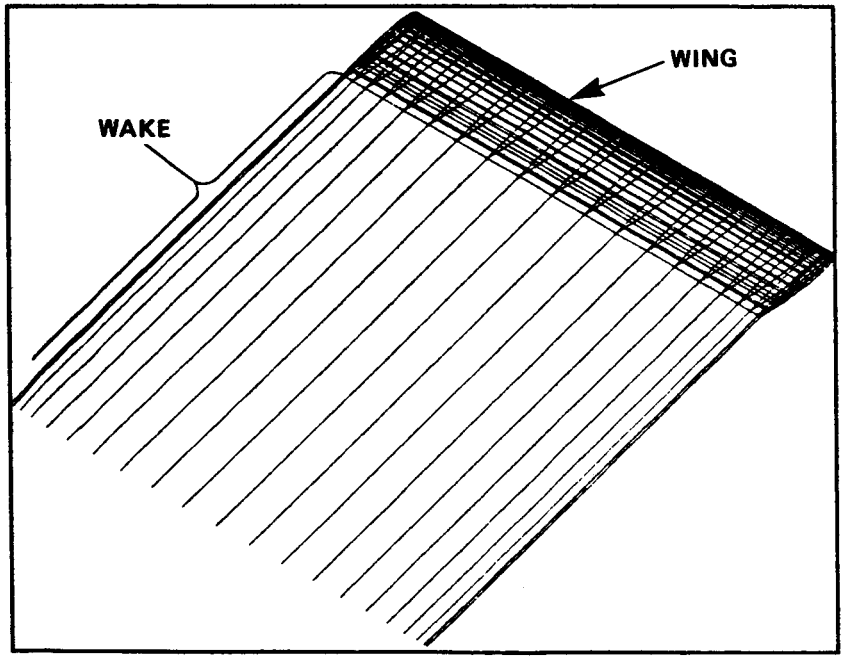

Figure 8.- Isometric View of Generating-Wing Panels prior to Wake Relaxation.

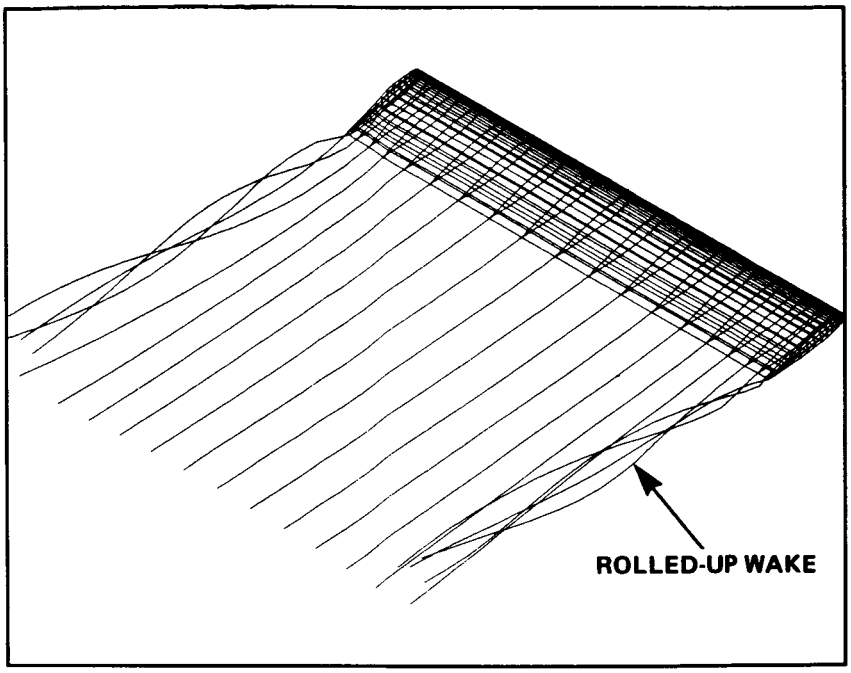

Figure 9.– Generating-Wing Wake after Relaxation.

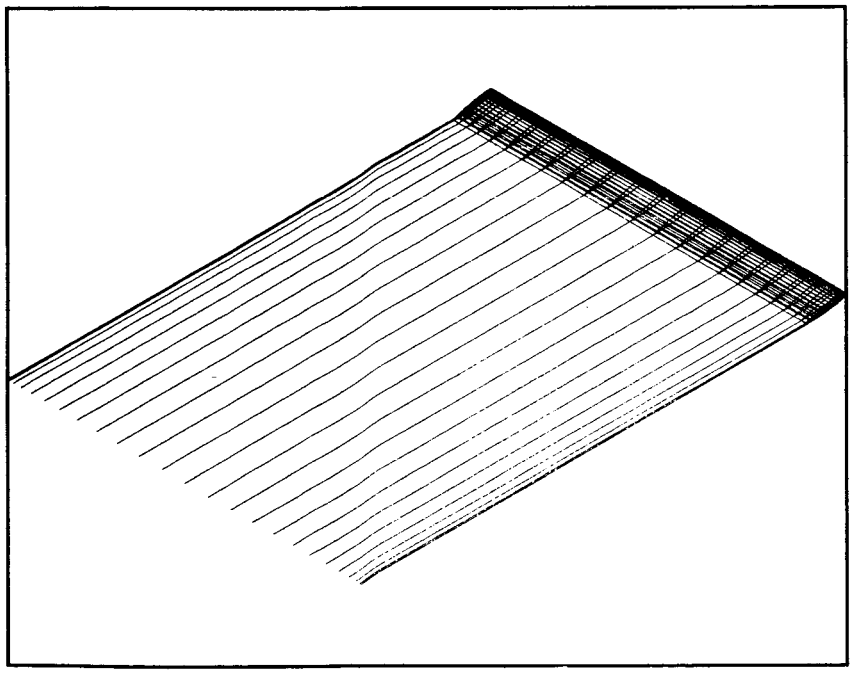

Figure 10.– Following-Wing Paneling.

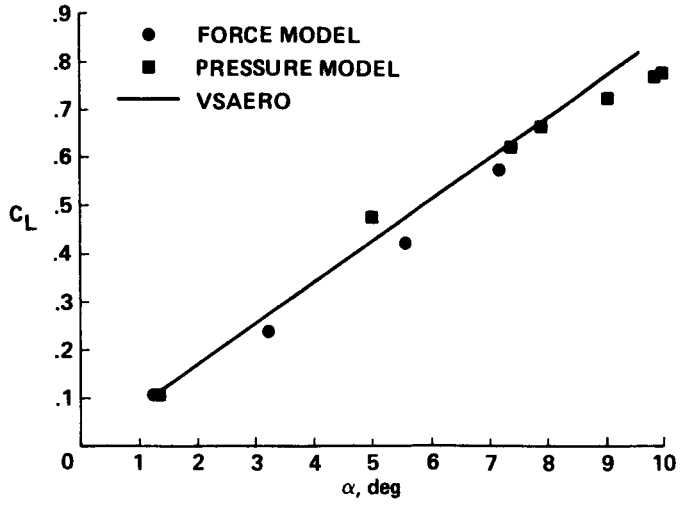

Figure 11.– Comparison of Experimental and Theoretical Lift Curves of the Following Wing.

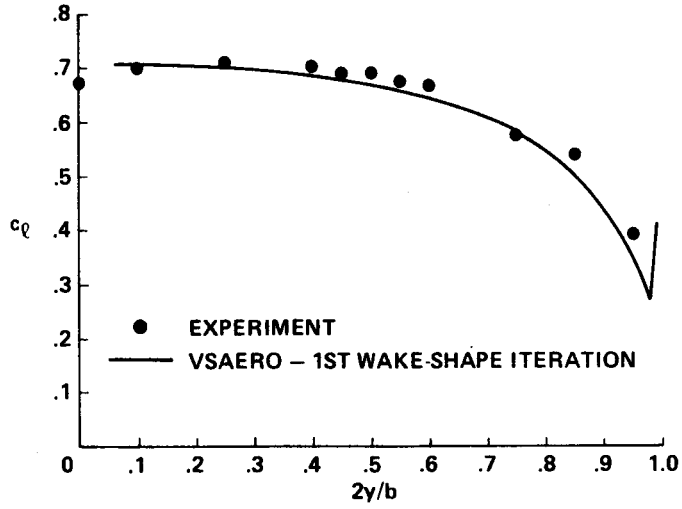

Figure 12.– Comparison of Experimental and Theoretical Span Loading of the Following Wing, $\alpha = 7.4°$.

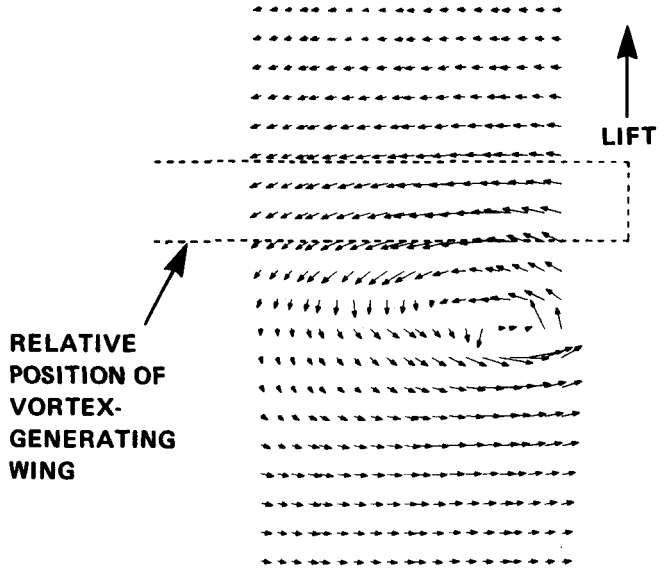

Figure 13.- Calculated Velocity Vectors at Two Generating-Wing Chordlengths, $x = 2c_g$, Downstream of the Generating-Wing Trailing Edge.

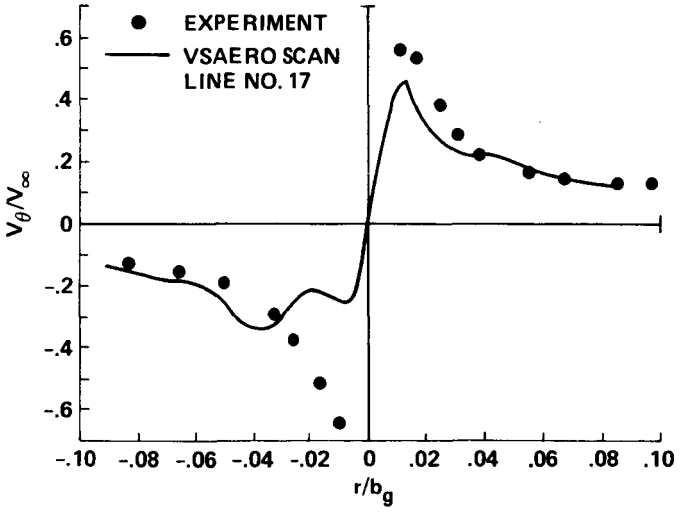

Figure 14.- Comparison of Experimental and Theoretical Vortex Tangential Velocities at $x = 2c_g$.

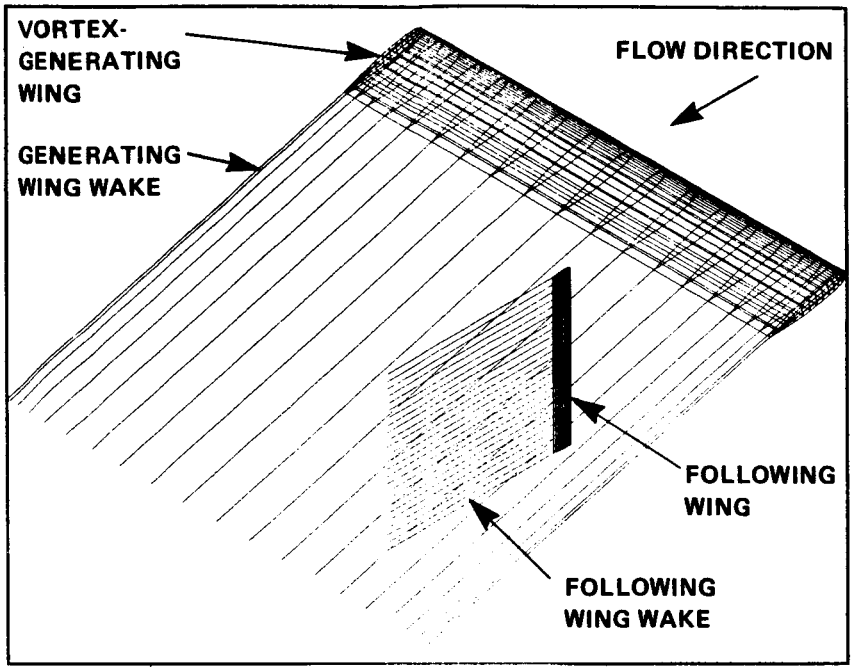

Figure 15.– Isometric View of Paneling and Initial Wake Configuration used for Simulation of the Experiment of reference 13.

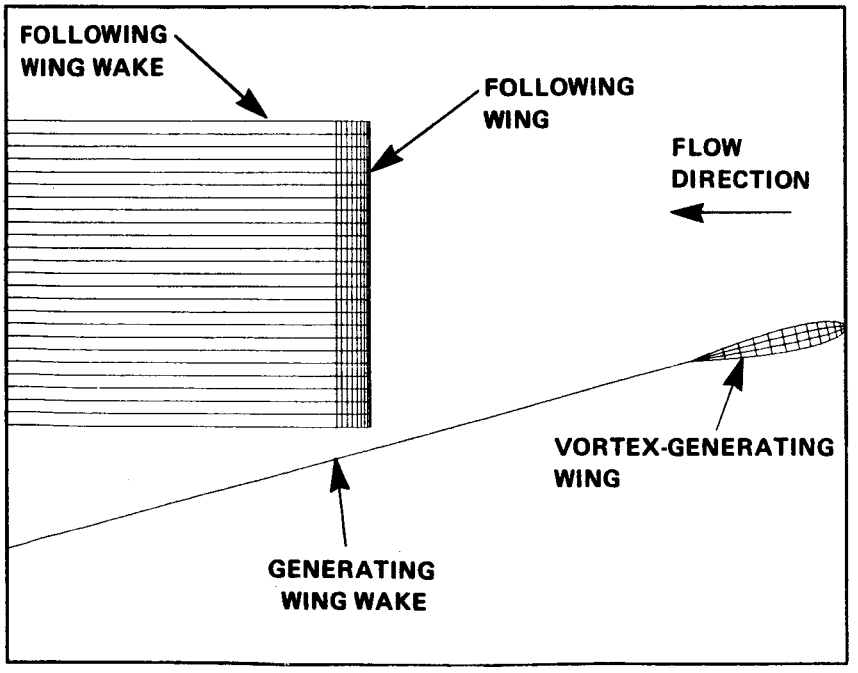

Figure 16.– Side View of Paneling and Initial Wake Configuration used for Simulation of the Experiment of reference 13.

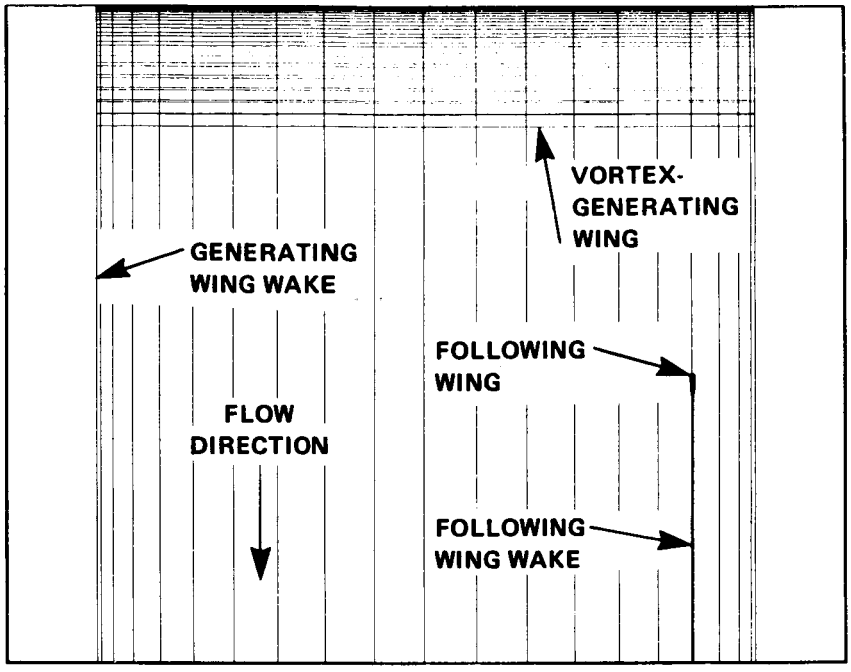

Figure 17.– Top View of Paneling and Initial Wake Configuration used for Simulation of the Experiment of reference 13.

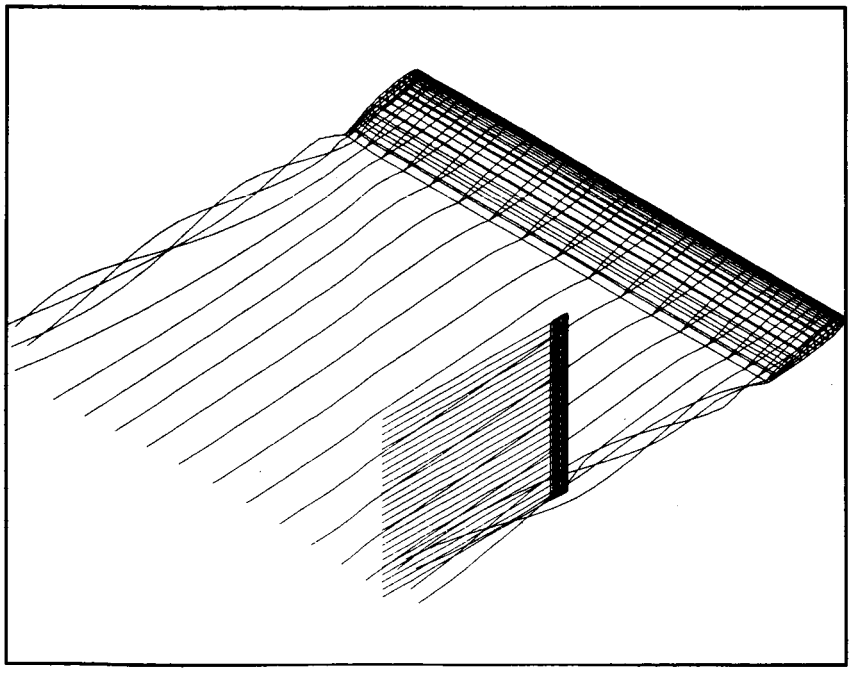

Figure 18.– Isometric View of Generating-Wing Wake after Four Wake-shape Iterations.

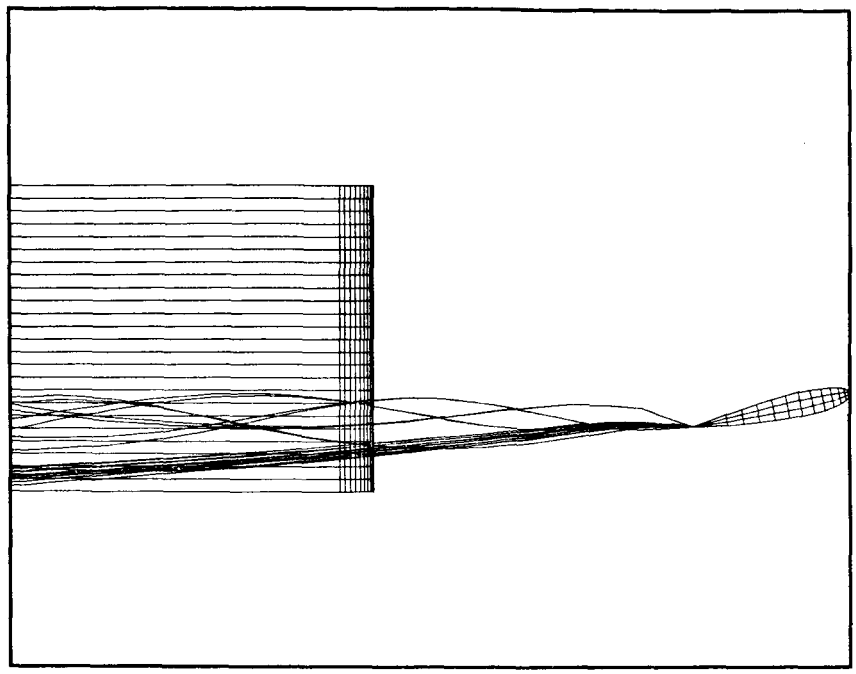

Figure 19.– Side View of Generating-Wing Wake after Four Wake-shape Iterations.

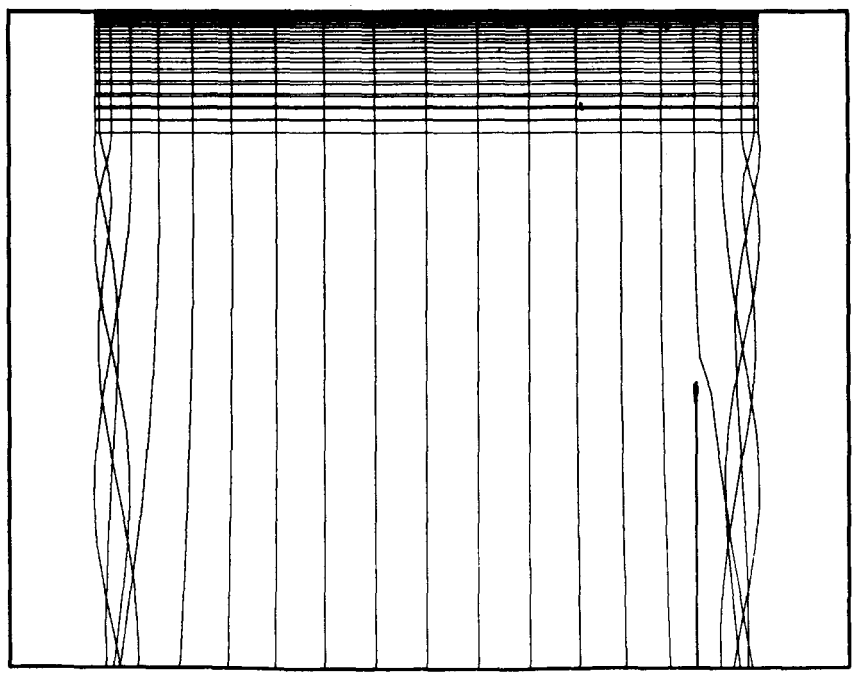

Figure 20.– Top View of Generating-Wing Wake after Four Wake-shape Iterations.

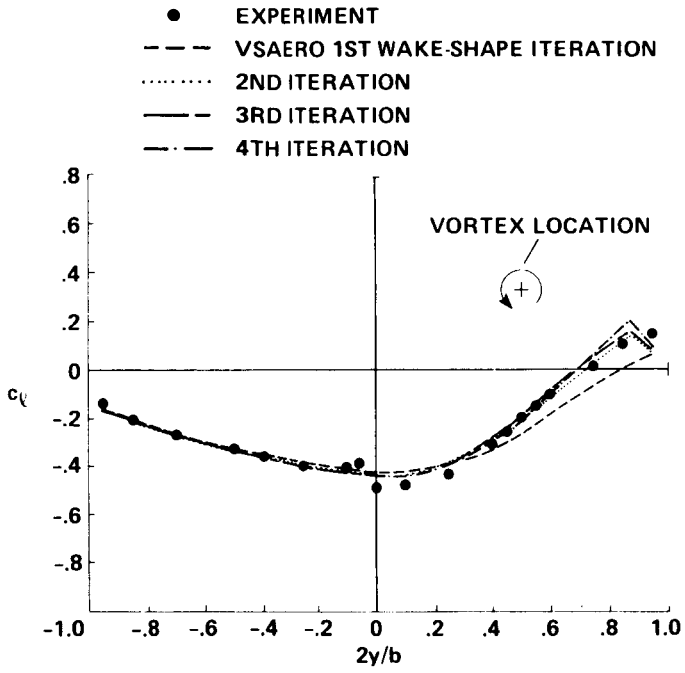

Figure 21.– Comparison of Experimental and Theoretical Span Loading on the Following Wing, $\frac{z_v}{c_f} = 1.73$.

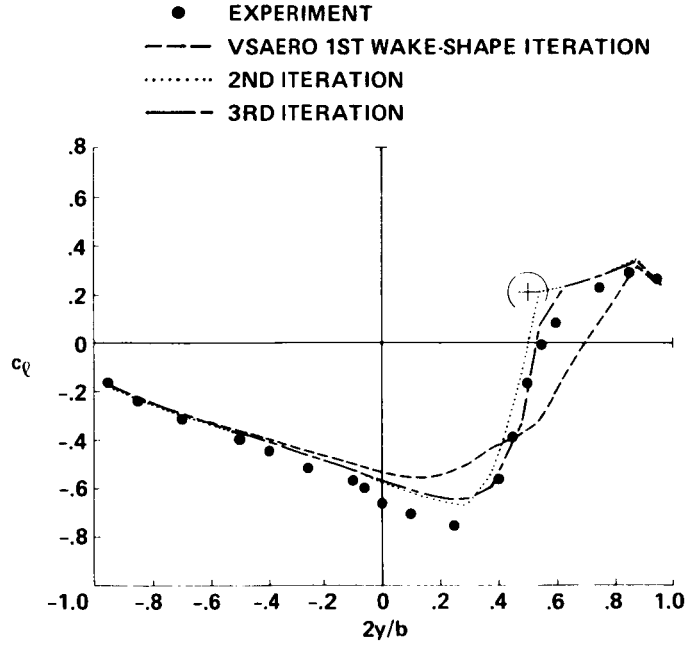

Figure 22.– Comparison of Experimental and Theoretical Span Loading on the Following Wing, $\frac{z_v}{c_f} = 0.73$.

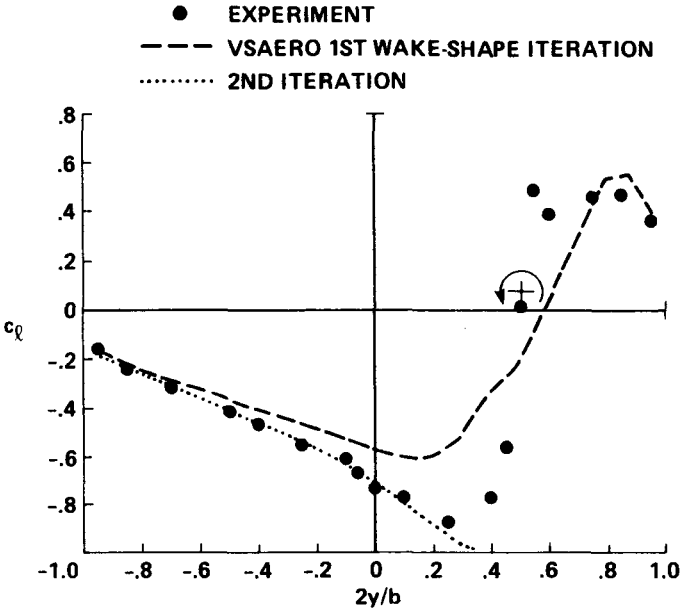

Figure 23.– Comparison of Experimental and Theoretical Span Loading on the Following Wing, $\frac{z_v}{c_f} = 0.23$.

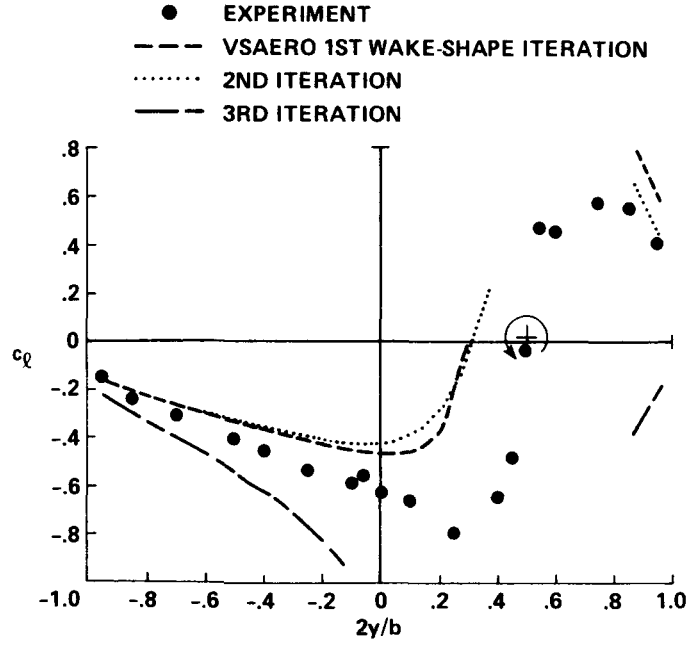

Figure 24.– Comparison of Experimental and Theoretical Span Loading on the Following Wing, $\frac{z_v}{c_f} = 0.05$.

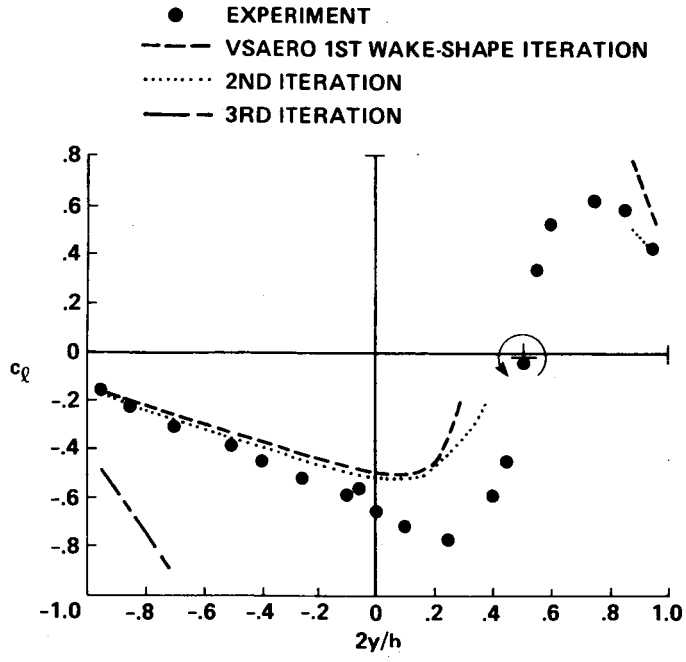

Figure 25.– Comparison of Experimental and Theoretical Span Loading on the Following Wing, $\frac{z_v}{c_f} = -0.02$.

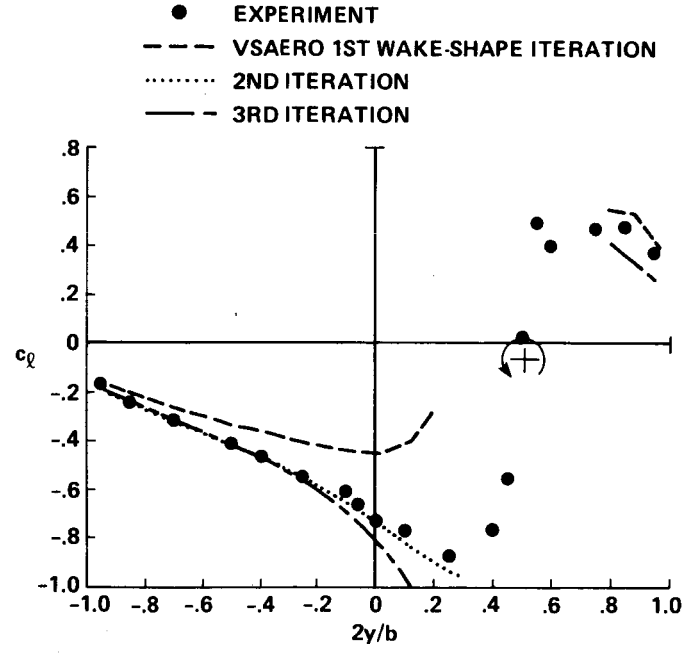

Figure 26.– Comparison of Experimental and Theoretical Span Loading on the Following Wing, $\frac{z_v}{c_f} = -0.18$.

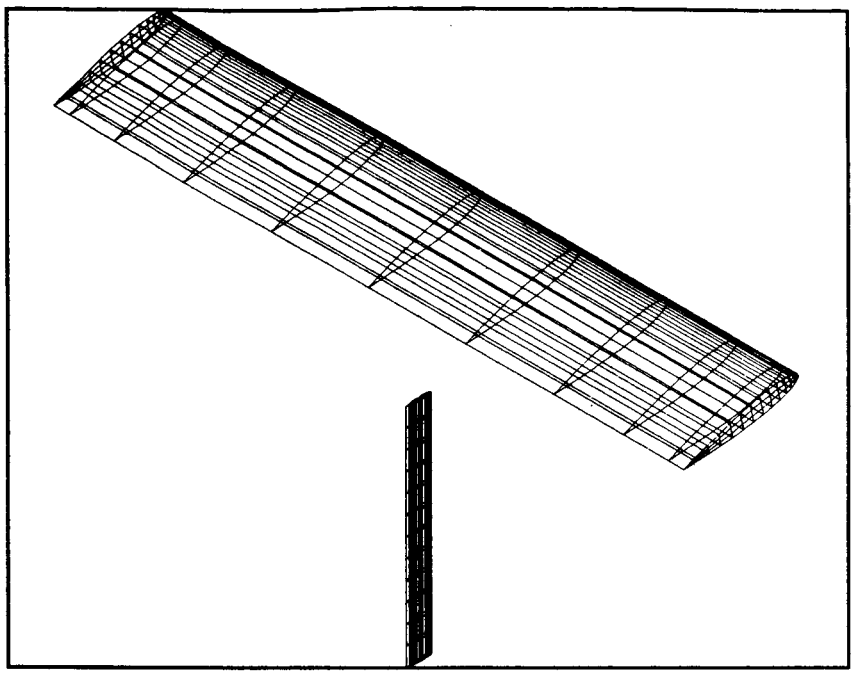

Figure 27.– First Modified Paneling Scheme used at $\frac{z_v}{c_f} = -0.02$.

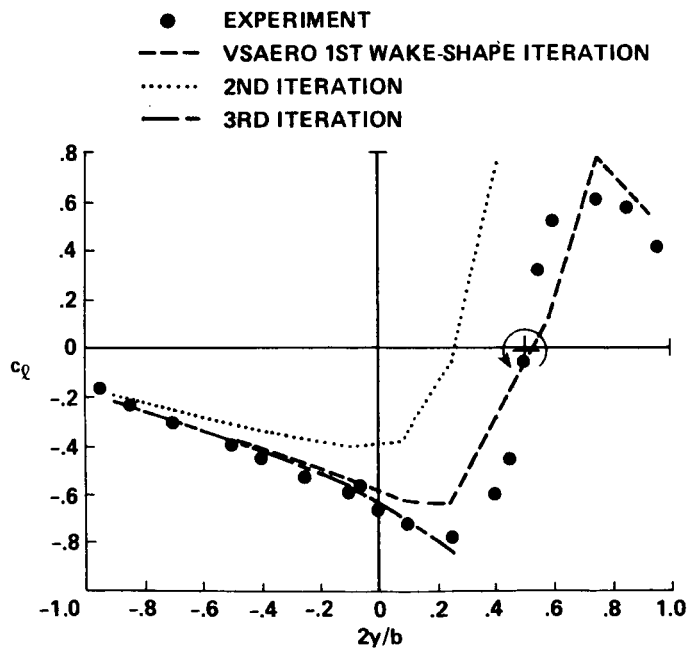

Figure 28.– Comparison of Experimental and Theoretical Span Loading on the Following Wing at $\frac{z_v}{c_f} = -0.02$ using First Modified Paneling Scheme.

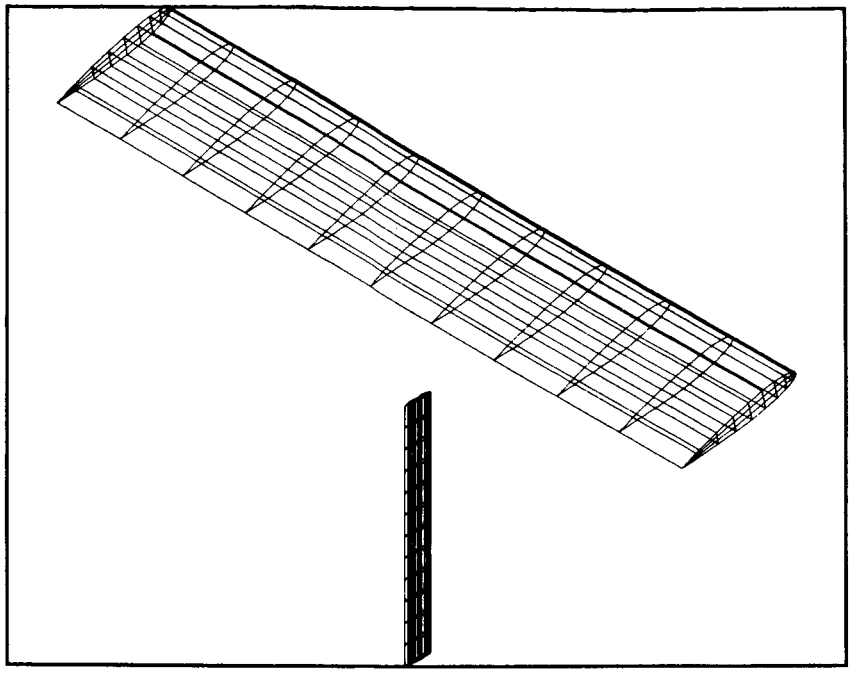

Figure 29.– Second Modified Paneling Scheme used at $\frac{z_v}{c_f} = -0.02$.

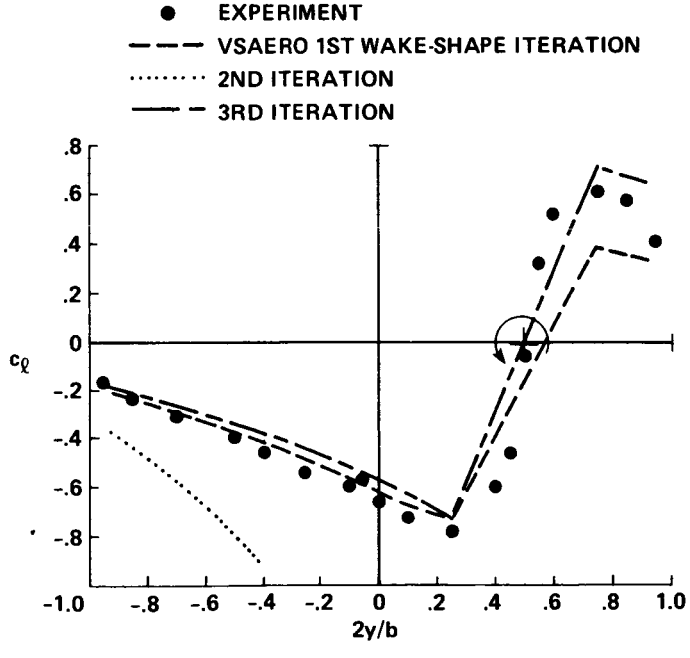

Figure 30.– Comparison of Experimental and Theoretical Span Loading on the Following Wing at $\frac{z_v}{c_f} = -0.02$ using Second Modified Paneling Scheme.

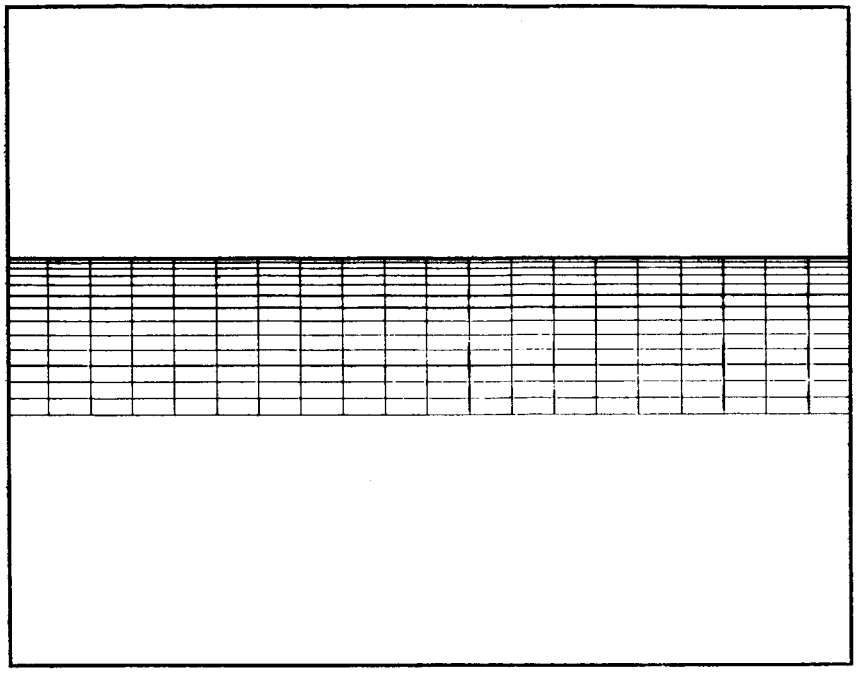

Figure 31.– Paneling used on the Generating Wing in Run 2.

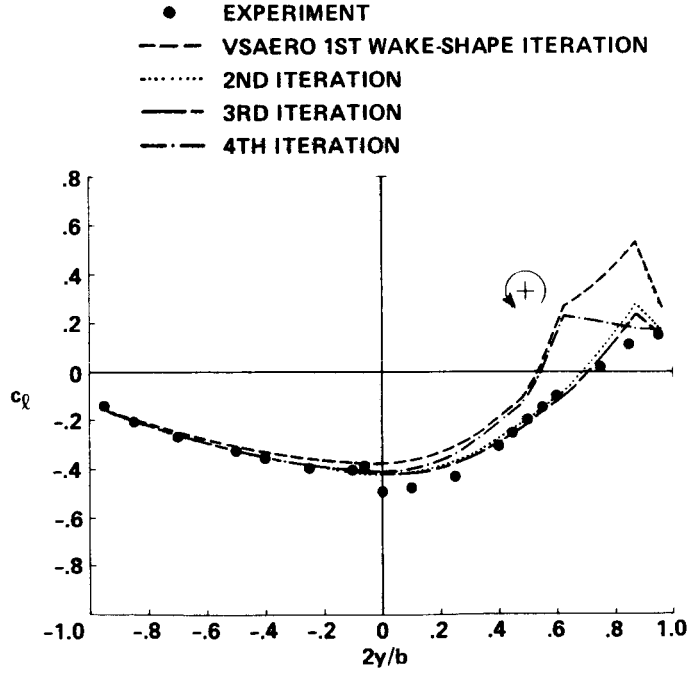

Figure 32.– Comparison of Experimental and Theoretical Span Loading on the Following Wing at $\frac{z_u}{c_f} = 1.73$ using Run 2 Paneling.

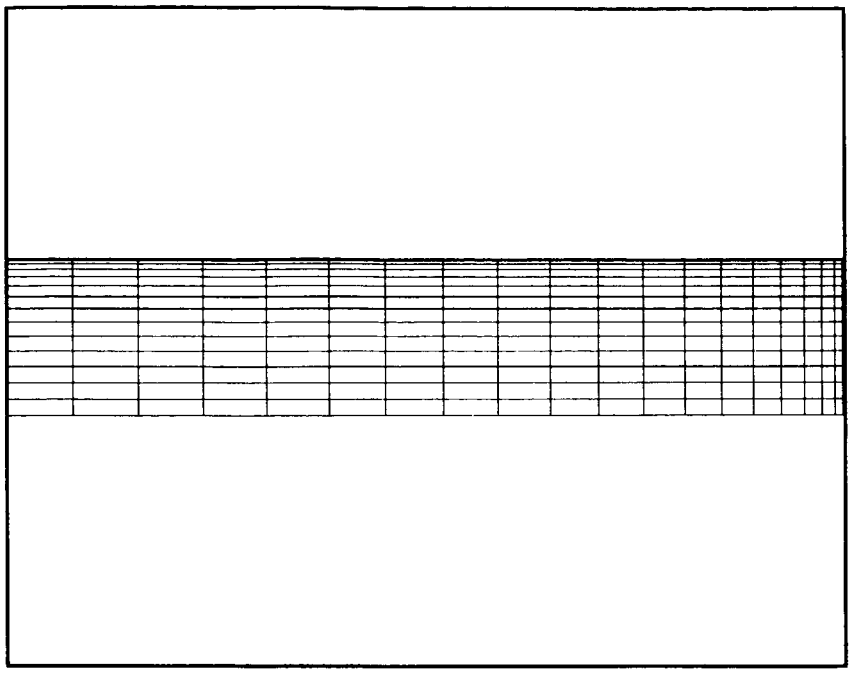

Figure 33.– Paneling used on the Generating Wing in Run 3.

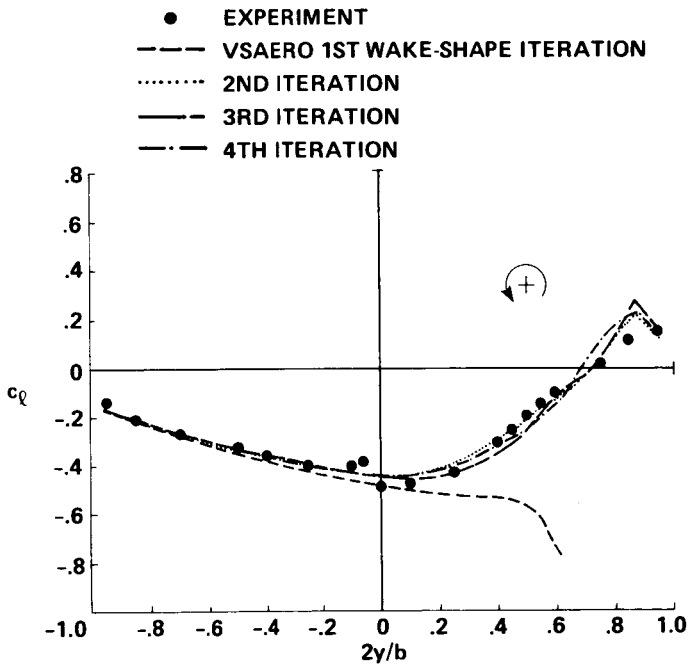

Figure 34.– Comparison of Experimental and Theoretical Span Loading on the Following Wing at $\frac{z_v}{c_f} = 1.73$ using Run 3 Paneling.

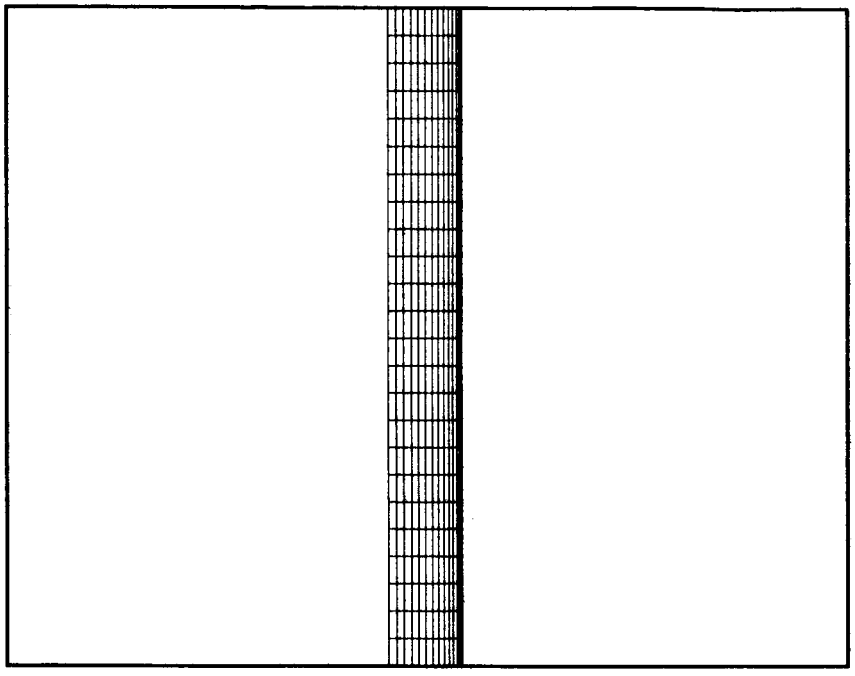

Figure 35.- Paneling used on the Following Wing in Run 4.

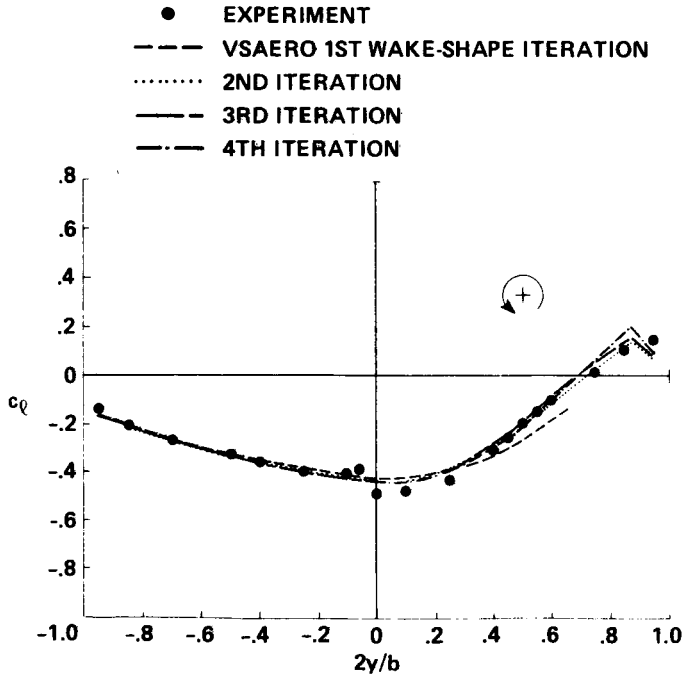

Figure 36.- Comparison of Experimental and Theoretical Span Loading on the Following Wing at $\frac{z_u}{c_f} = 1.73$ using Run 4 Paneling.

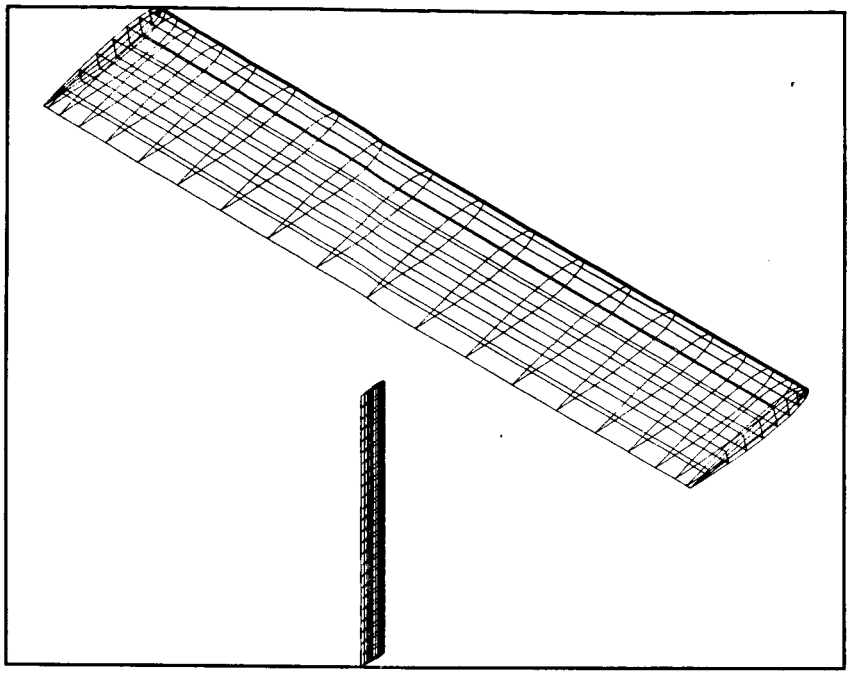

Figure 37.– Isometric View of Run 5 Paneling.

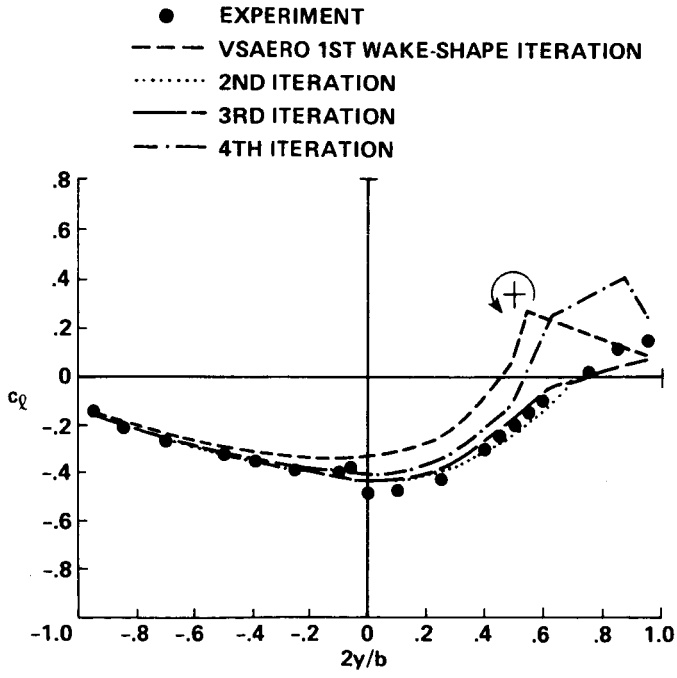

Figure 38.– Comparison of Experimental and Theoretical Span Loading on the Following Wing at $\frac{z_v}{c_f} = 1.73$ using Run 5 Paneling.

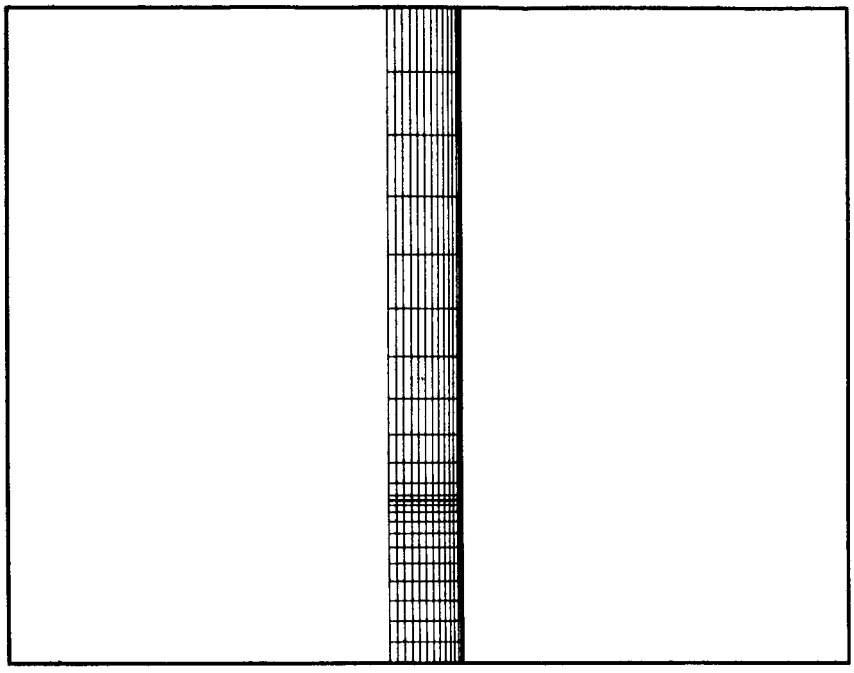

Figure 39.- Spanwise Panel Distribution used on the Following Wing in Run 6.

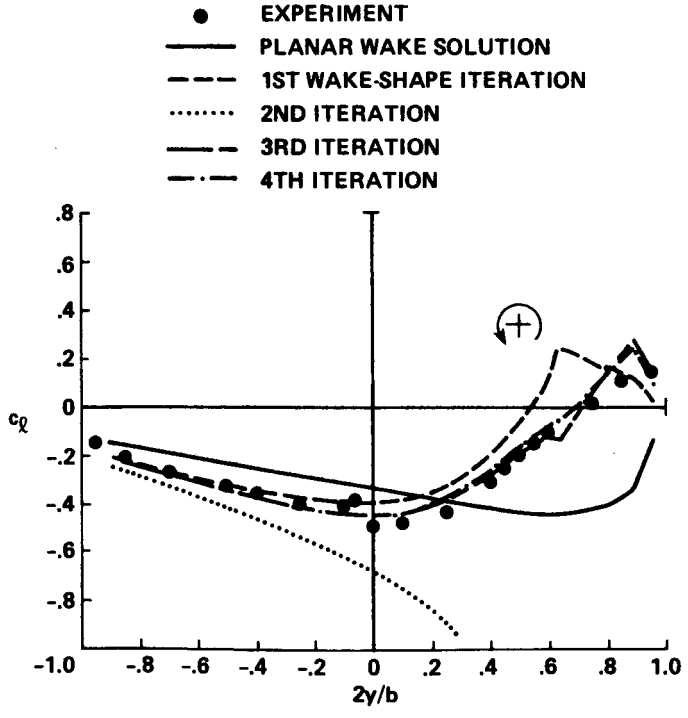

Figure 40.- Comparison of Experimental and Theoretical Span Loading on the Following Wing at $\frac{z_v}{c_f} = 1.73$ using Run 6 Paneling.

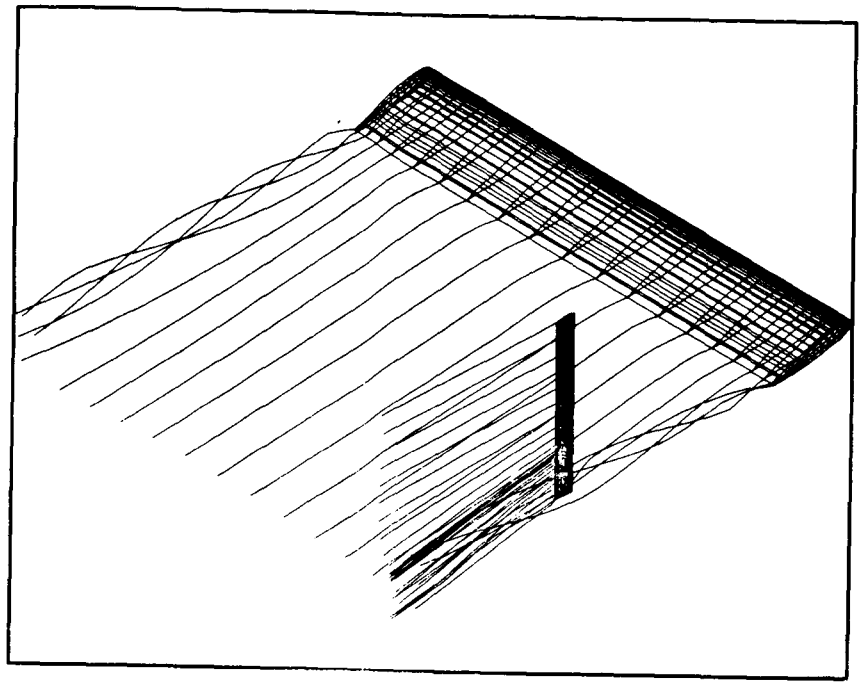

Figure 41.– Isometric View of Wake Vortex Filaments after Final Wake-Shape Iteration of Run 7.

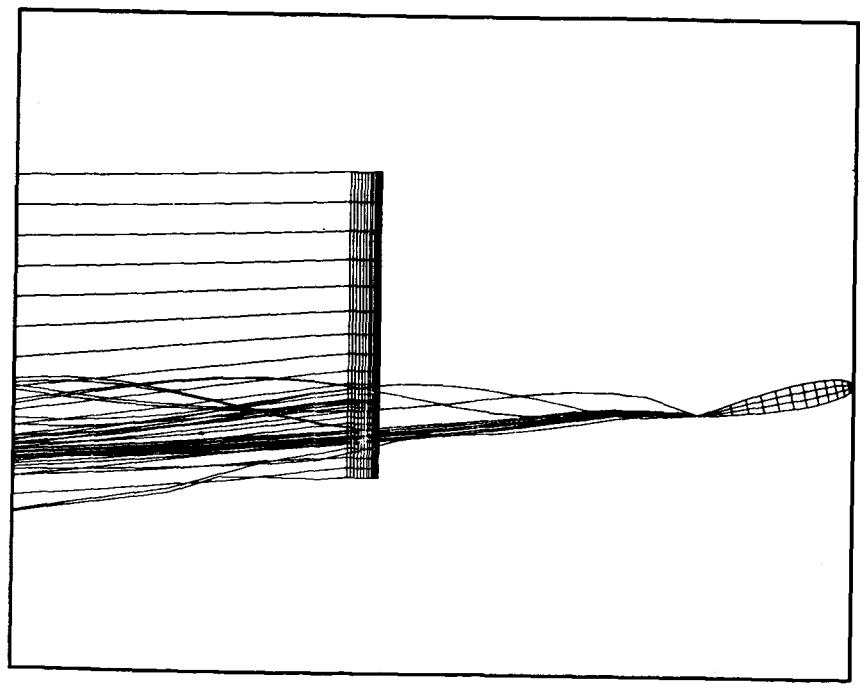

Figure 42.– Side View of Wake Vortex Filaments after Final Wake-Shape Iteration of Run 7.

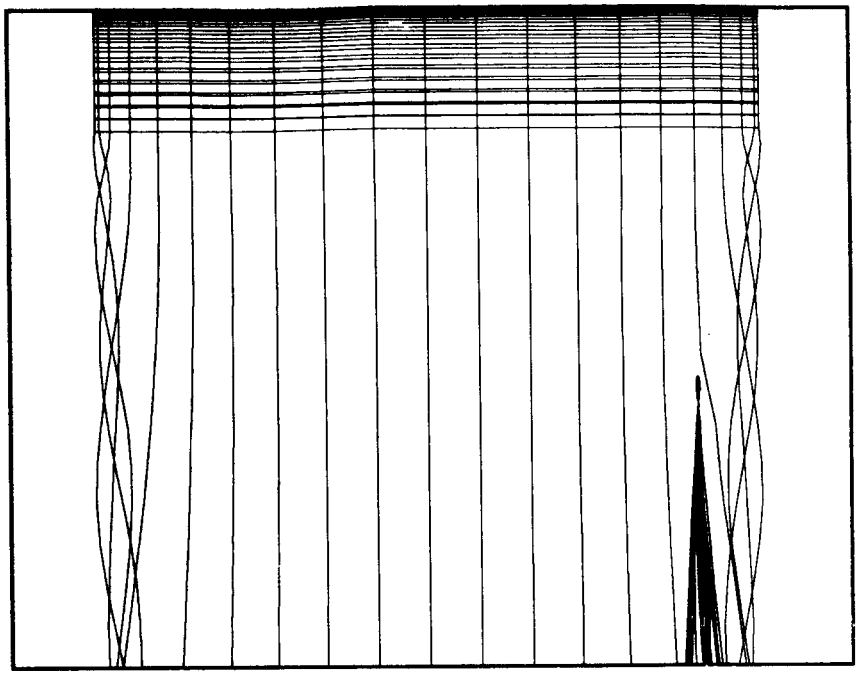

Figure 43.- Top View of Wake Vortex Filaments after Final Wake-Shape Iteration of Run 7.

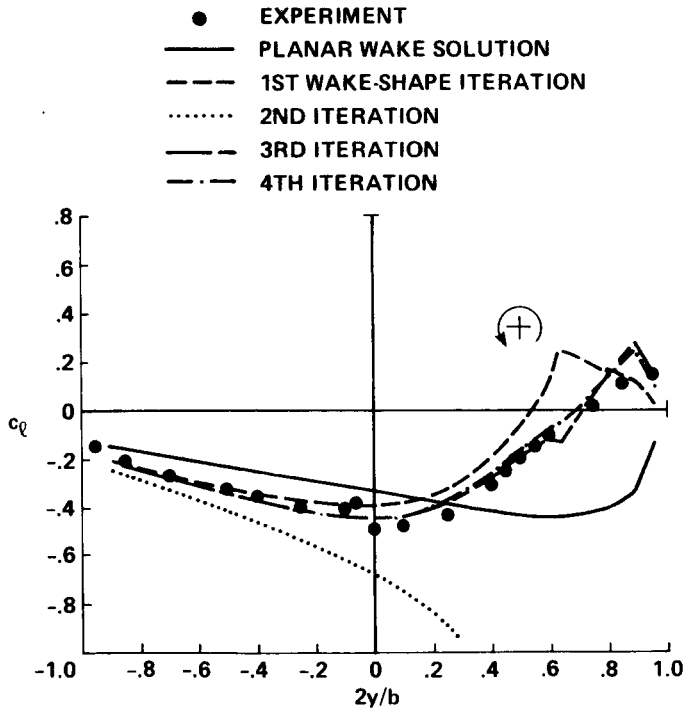

Figure 44.- Comparison of Experimental and Theoretical Span. Loading on the Following Wing at $\frac{z_v}{c_f} = 1.73$ using Run 7 Relaxed Following-Wing Wake.

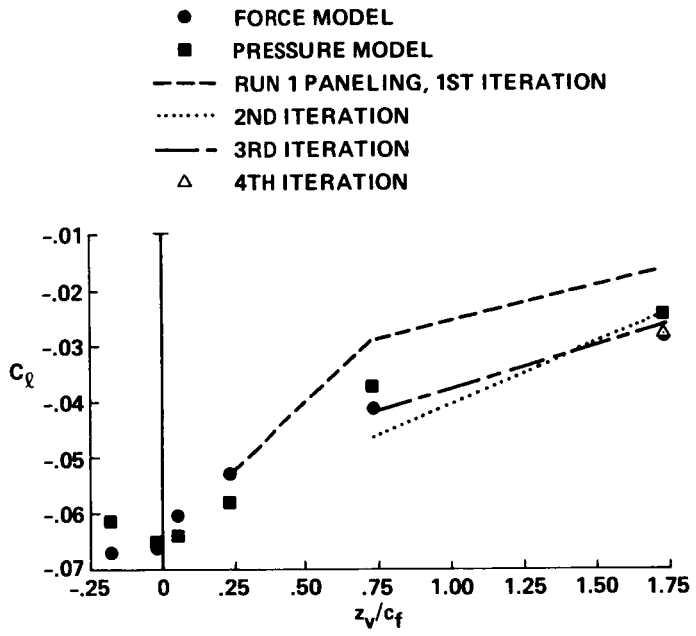

Figure 45.– Comparison of Experimental and Theoretical Rolling-Moment Coefficients on the Following Wing.

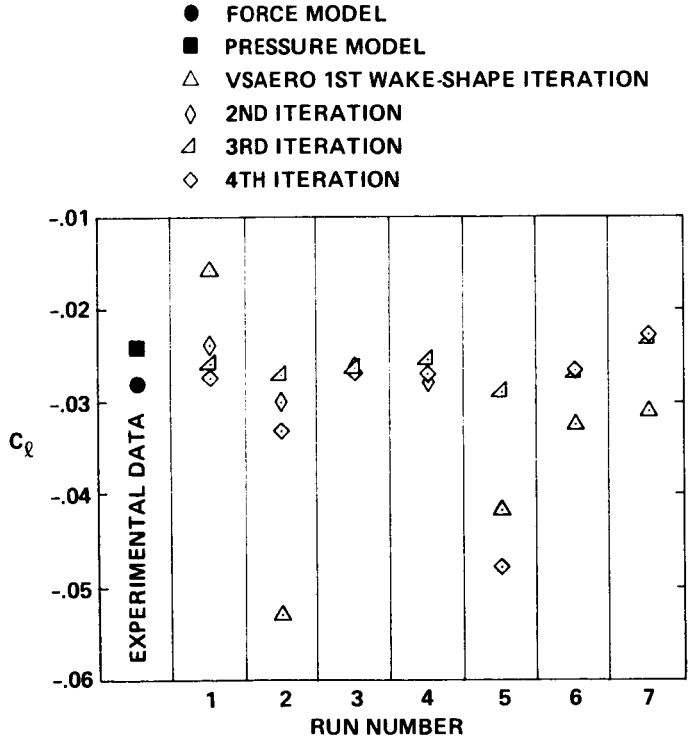

Figure 46.– Comparison of Experimental and Theoretical Rolling-Moment Coefficients on the Following Wing for Runs 1 through 7.

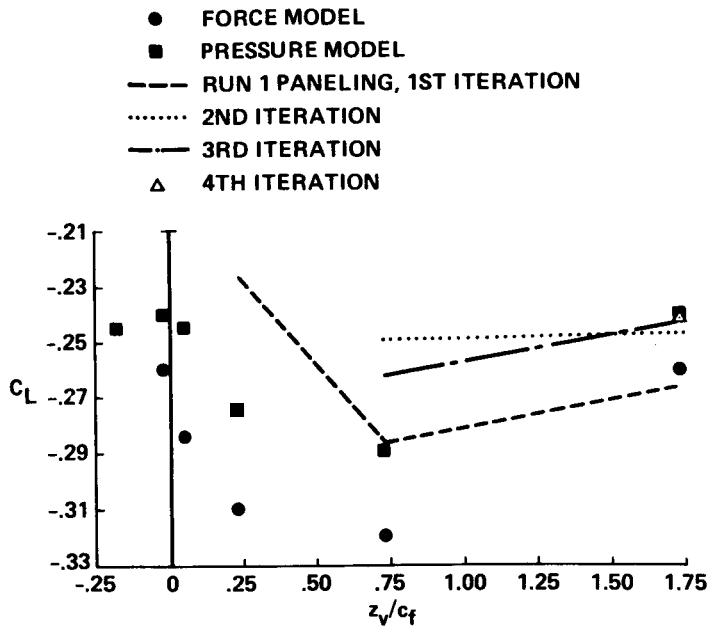

Figure 47.- Comparison of Experimental and Theoretical Lift Coefficients on the Following Wing.

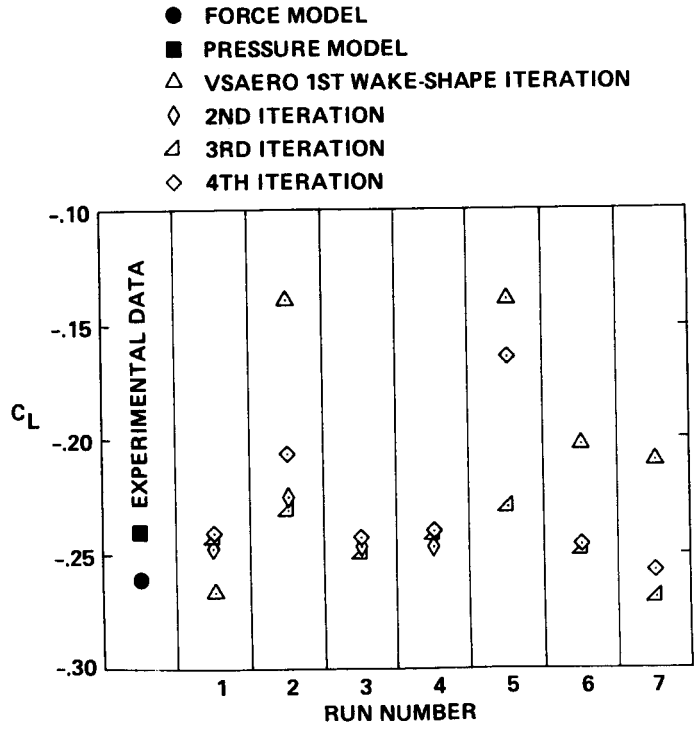

Figure 48.- Comparison of Experimental and Theoretical Lift Coefficients on the Following Wing for Runs 1 through 7.

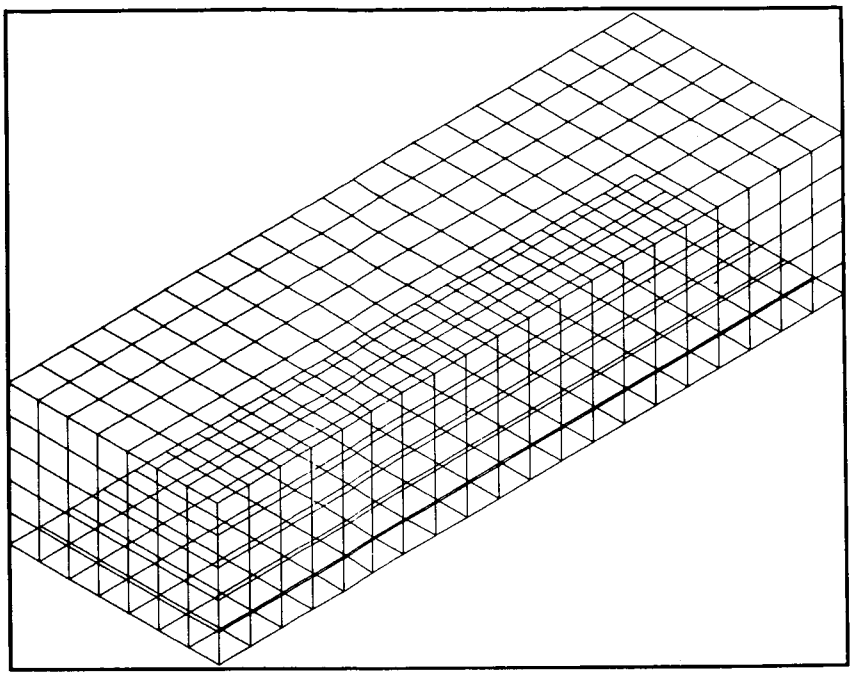

Figure 49.– Isometric View of Duct used in Simulations of the Experiment of reference 14.

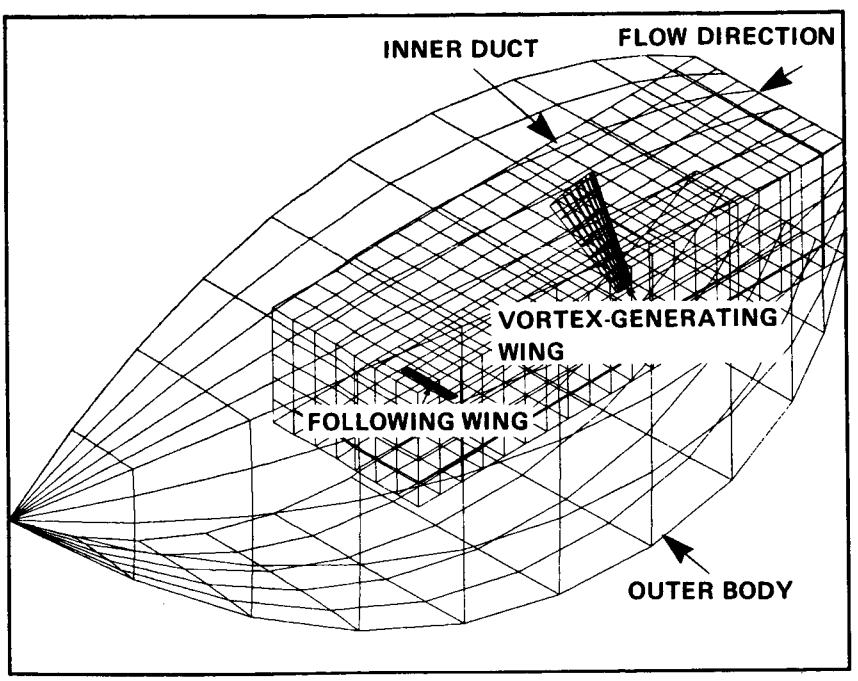

Figure 50.– Isometric View of Entire Tunnel Configuration and Wings used in Simulations of the Experiment of reference 14.

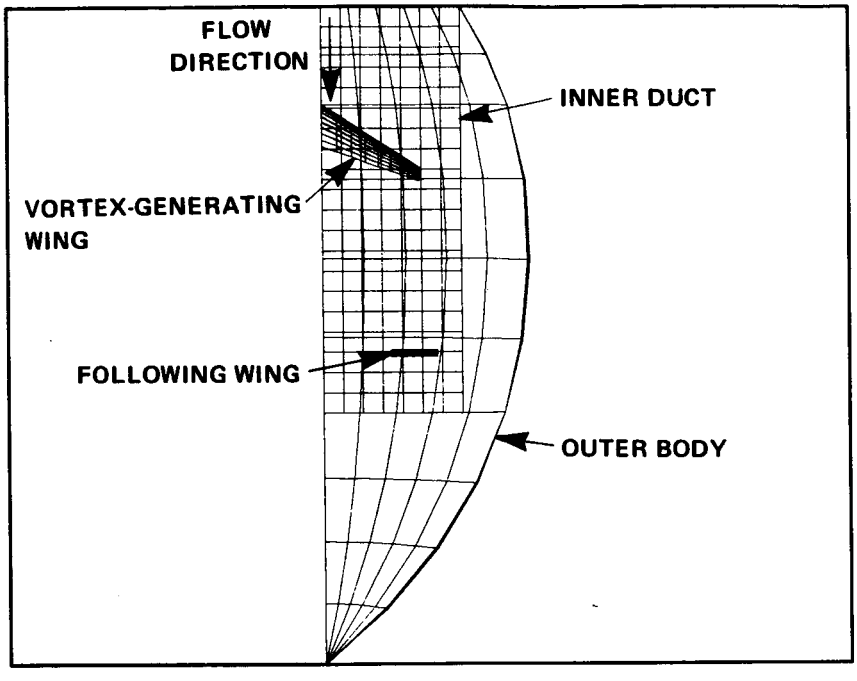

Figure 51.– Side View of Entire Tunnel Configuration and Wings used in the Simulation of the Experiment of reference 14.

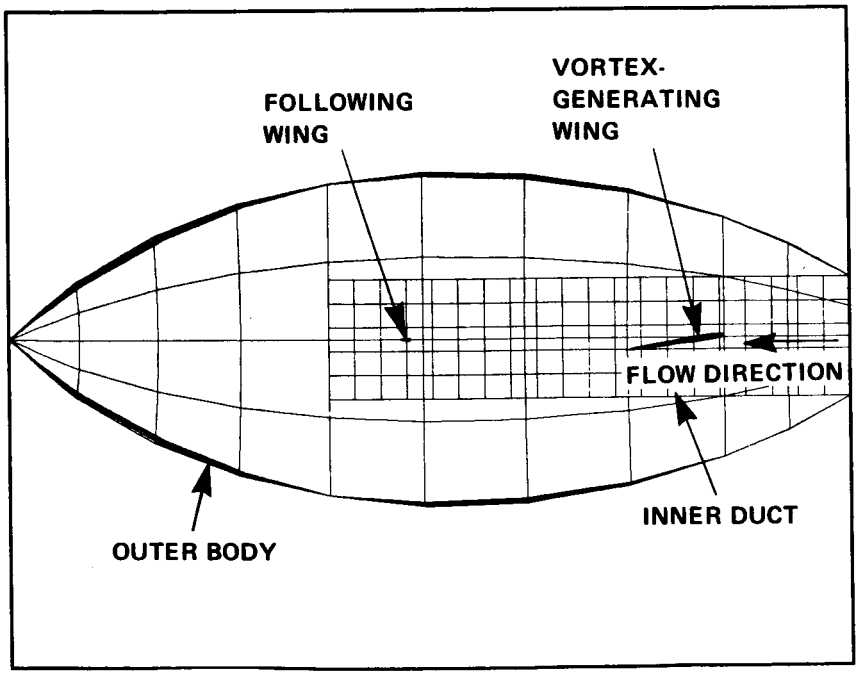

Figure 52.– Top View of Entire Tunnel Configuration and Wings used in the Simulation of the Experiment of reference 14.

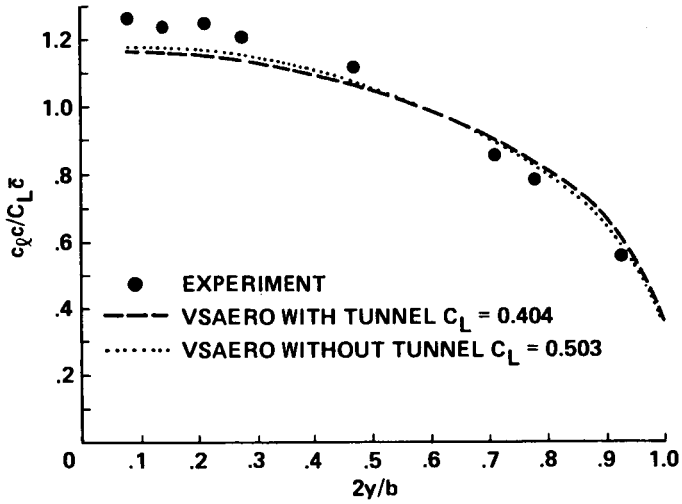

Figure 53.– Comparison of Experimental and Theoretical Span Loading on the Generating Wing at $\alpha = 6.25°$.

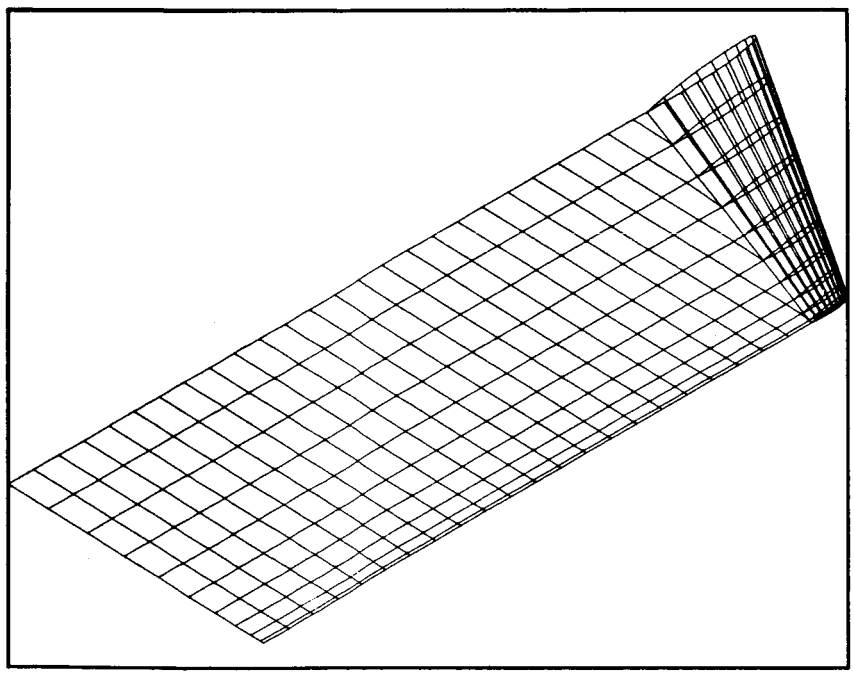

Figure 54.– Isometric View of Generating Wing and Wake Paneling.

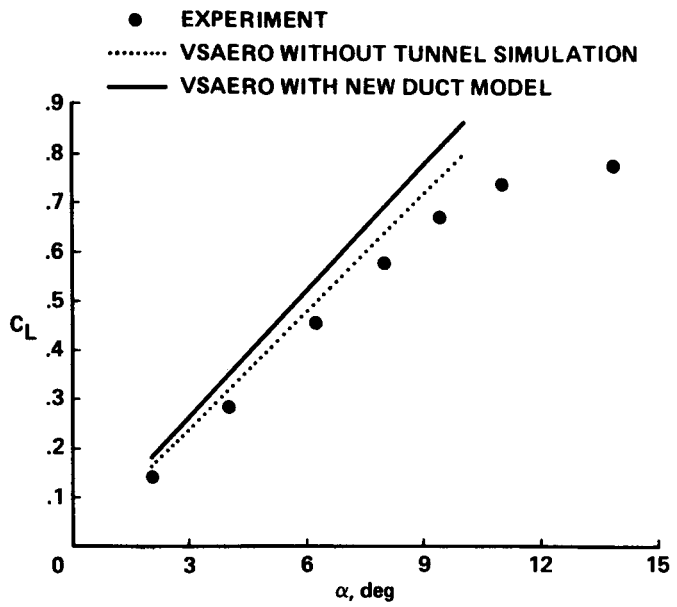

Figure 55.– Comparison of Experimental and Theoretical Lift Curve of the Generating Wing.

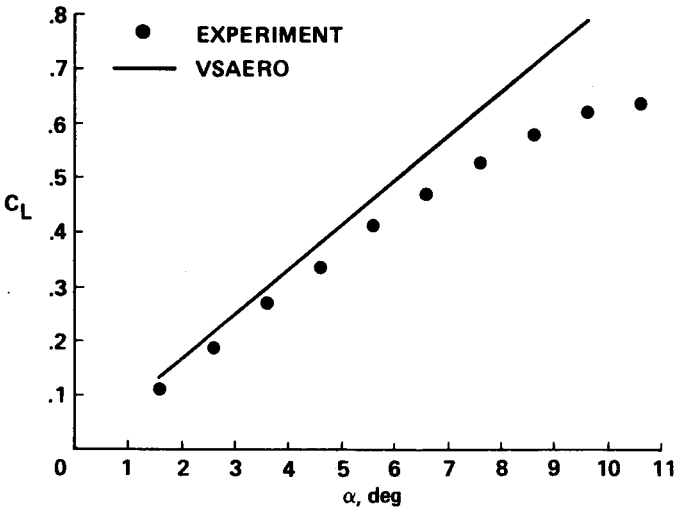

Figure 56.– Comparison of Experimental and Theoretical Lift Curve of the Following Wing.

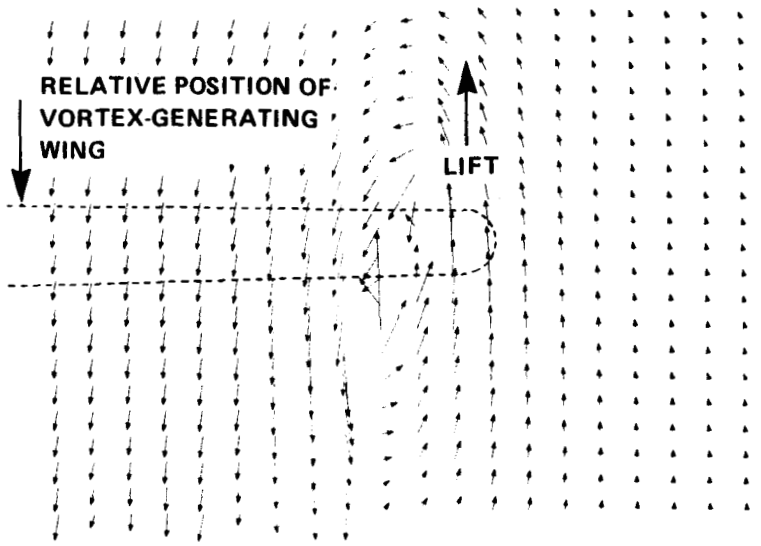

Figure 57.– Calculated Velocity Vectors at $x = 2.5b_g$.

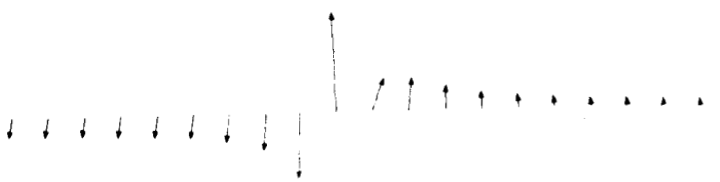

Figure 58.– Velocity Vectors of Scan Line 13.

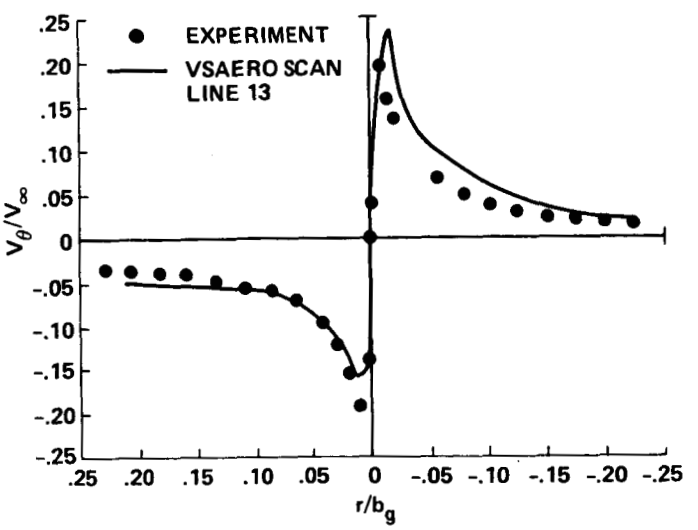

Figure 59.– Comparison of Experimental and Theoretical Vortex Tangential Velocities at $x = 2.5b_g$.

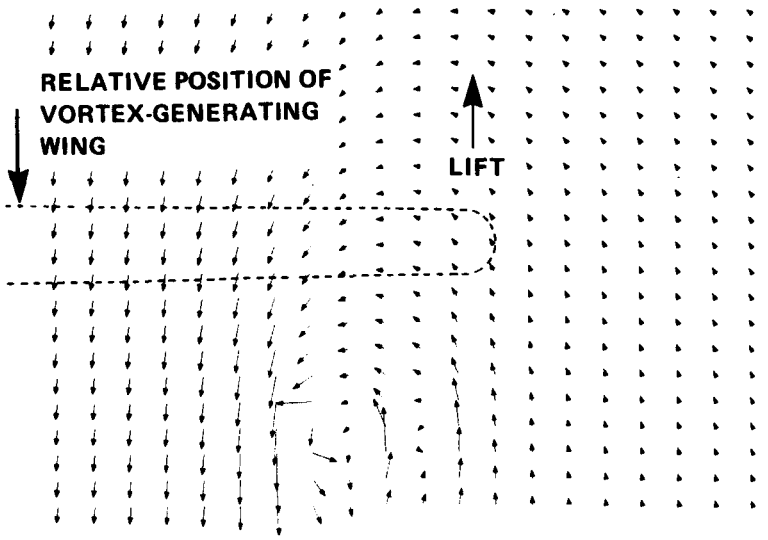

Figure 60.– Calculated Velocity Vectors at $x = 5.0b_g$.

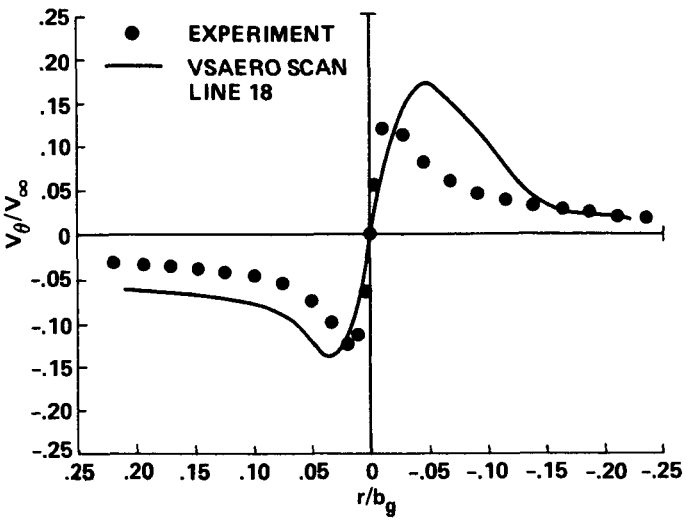

Figure 61.– Comparison of Experimental and Theoretical Vortex Tangential Velocities at $x = 5.0b_g$.

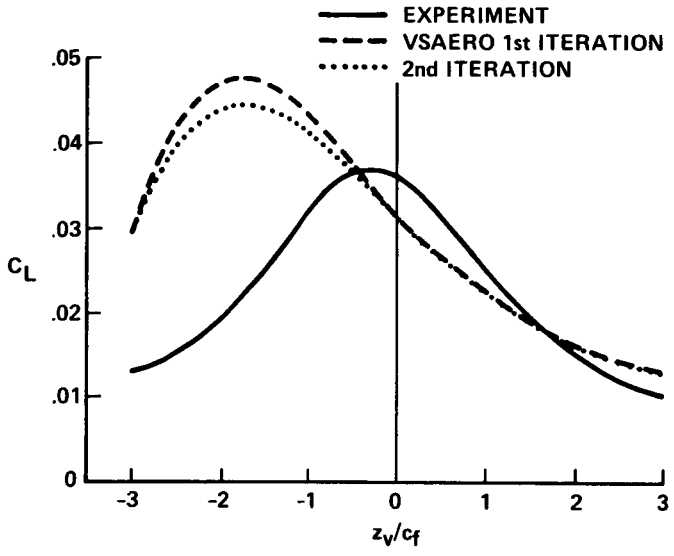

Figure 62.- Comparison of Experimental and Theoretical Rolling-Moment Coefficients on the Following Wing at $x = 2.5b_g$.

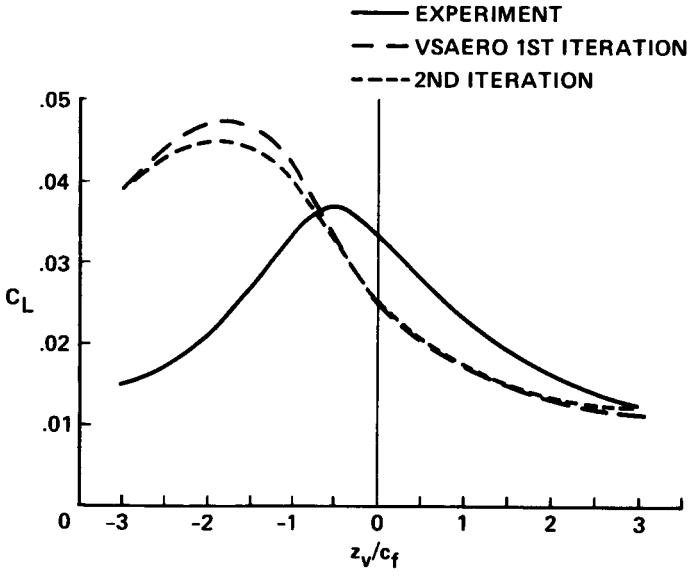

Figure 63.- Comparison of Experimental and Theoretical Rolling-Moment Coefficients on the Following Wing at $x = 5.0b_g$.

NASA National Aeronautics and Space Administration

Report Documentation Page

1. Report No.	2. Government Accession No.	3. Recipient's Catalog No.
NASA TM-88337		

4. Title and Subtitle

Application of a Panel Method to Wake-Vortex/ Wing Interaction and Comparison with Experimental Data

5. Report Date

September 1987

6. Performing Organization Code

7. Author(s)

Brian E. Smith and James C. Ross

8. Performing Organization Report No.

A-86330

10. Work Unit No.

505-60-21

9. Performing Organization Name and Address

Ames Research Center
Moffett Field, CA 94035

11. Contract or Grant No.

13. Type of Report and Period Covered

Technical Memorandum

12. Sponsoring Agency Name and Address

National Aeronautics and Space Administration
Washington, DC 20546-0001

14. Sponsoring Agency Code

15. Supplementary Notes

Point of Contact: Brian E. Smith, Ames Research Center, M/S 247-1
Moffett Field, CA 94035 (415) 694-5039 or FTS 464-5039

16. Abstract

The ability of the VSAERO (an acronym for Vortex Separation AEROdynamics) program to calculate aerodynamic loads on wings due to interaction with free vortices was studied. The loads were calculated for various positions of a downstream following wing relative to an upstream vortex-generating wing. Calculated vortex-induced span loads, rolling-moment coefficients, and lift coefficients on the following wing were compared with experimental results of McMillan et al. and El-Ramly et al. Comparisons of calculated and experimental vortex tangential velocities were also made.

17. Key Words (Suggested by Author(s))	18. Distribution Statement
Panel method VSAERO Rolling moment	Unclassified-Unlimited Subject Category - 02

19. Security Classif. (of this report)	20. Security Classif. (of this page)	21. No. of pages	22. Price
Unclassified	Unclassified	64	A04